Paths and wakes of deformable nearly spheroidal rising bubbles close to the transition to path instability

José Carlos Cano-Lozano and Carlos Martínez-Bazán
Área de Mecánica de Fluidos, Departamento de Ingeniería Mecánica y Minera, Universidad de Jaén, Campus de las Lagunillas, 23071 Jaén, Spain

Jacques Magnaudet
Institut de Mécanique des Fluides de Toulouse, Université de Toulouse, CNRS, INPT, UPS, 31062 Toulouse, France

Joël Tchoufag
Institut de Mécanique des Fluides de Toulouse, Université de Toulouse, CNRS, INPT, UPS, 31062 Toulouse, France
and Department of Mechanical Engineering, University of California, Berkeley, Berkeley, California 94720, USA

We report on a series of results provided by three-dimensional numerical simulations of nearly spheroidal bubbles freely rising and deforming in a still liquid in the regime close to the transition to path instability. These results improve upon those of recent computational studies [Cano-Lozano *et al.*, Int. J. Multiphase Flow **51**, 11 (2013); Phys. Fluids **28**, 014102 (2016)] in which the neutral curve associated with this transition was obtained by considering realistic but frozen bubble shapes. Depending on the dimensionless parameters that characterize the system, various paths geometries are observed by letting an initially spherical bubble starting from rest rise under the effect of buoyancy and adjust its shape to the surrounding flow. These include the well-documented rectilinear axisymmetric, planar zigzagging, and spiraling (or helical) regimes. A flattened spiraling regime that most often eventually turns into either a planar zigzagging or a helical regime is also frequently observed. Finally, a chaotic regime in which the bubble experiences small horizontal displacements (typically one order of magnitude smaller than in the other regimes) is found to take place in a region of the parameter space where no standing eddy exists at the back of the bubble. The discovery of this regime provides evidence that path instability does not always result from a wake instability as previously believed. In each regime, we examine the characteristics of the path, bubble shape, and vortical structure in the wake, as well as their couplings. In particular, we observe that, depending on the fluctuations of the rise velocity, two different vortex shedding modes exist in the zigzagging regime, confirming earlier findings with falling spheres. The simulations also reveal that significant bubble deformations may take place along zigzagging or spiraling paths and that, under certain circumstances, they dramatically alter the wake structure. The instability thresholds that can be inferred from the computations compare favorably with experimental data provided by various sets of recent experiments guaranteeing that the bubble surface is free of surfactants.

DOI: 10.1103/PhysRevFluids.1.053604

I. INTRODUCTION

The phenomenon in which the path of a bubble rising in a still liquid stops following a straight vertical line and switches to a zigzag or helical trajectory is familiar to everybody and became known at some point in the scientific community as Leonardo's paradox [1]. This phenomenon, in which the bubble shape, path, and wake are intimately coupled, has been widely studied since the 1950s,

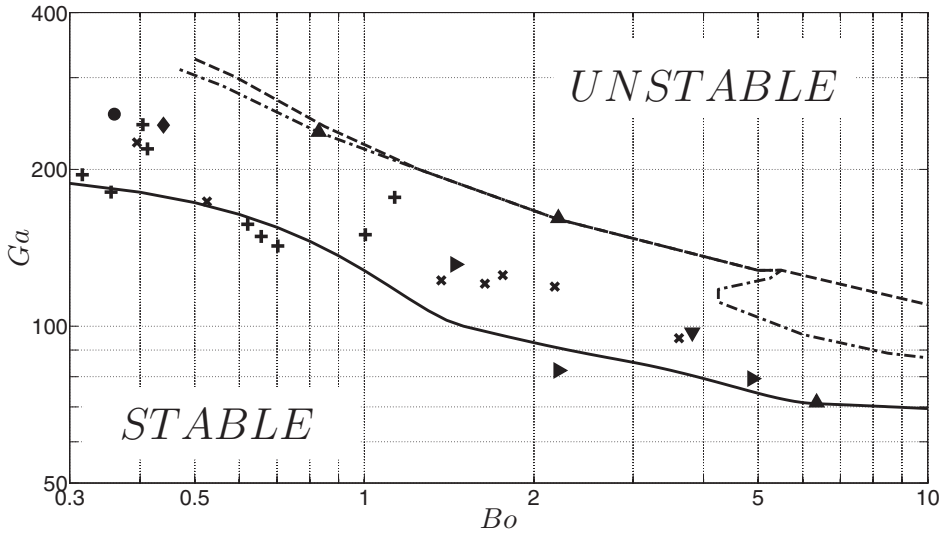

FIG. 1. Phase diagram in the (Bo,Ga) plane: solid line, approximate critical curve determined from three-dimensional simulations performed using frozen realistic bubble shapes in Ref. [23]; dash-dotted and dashed lines, critical curves obtained in Ref. [24] using the LSA approach with a freely moving and a fixed bubble, respectively; and symbols, experimental data corresponding to incipient path instability observed in various liquids (+ [12], × [13], • [4], ♦ [14], ▲ [9], ▼ [10], and ► [11]).

although the bubble hydrodynamic behavior is far from being fully understood yet. The first modern study focused on that problem was performed by Haberman and Morton [2], using various liquids. Depending on the bubble size, their study identified three different types of paths, namely, rectilinear, spiral, and straight rocking. Afterward, many experimental studies were performed to analyze the bubble shape, terminal velocity, wake, and path (see, for instance, [3–6] and references therein). The transition from a rectilinear to an oscillatory path was specifically examined in Refs. [4,5,7–14]. Some of the corresponding results are displayed in Fig. 1 in the (Bo,Ga) plane, where Bo and Ga are, respectively, the Bond number $\mathrm{Bo} = \rho g D^2/\sigma$ and the Galilei number $\mathrm{Ga} = \rho g^{1/2} D^{3/2}/\mu$, with ρ, μ, and σ denoting the density, viscosity, and surface tension of the liquid, respectively, D being the bubble equivalent diameter and g the gravitational acceleration. Eliminating D in between the Galilei and Bond numbers yields the so-called Morton number $\mathrm{Mo} = \mathrm{Bo}^3/\mathrm{Ga}^4 = g\mu^4/\rho\sigma^3$; hence only two out of these three numbers are enough to entirely characterize the system provided the density and viscosity of the liquid are much larger than those of the gas that fills the bubble. For each value of Bo, the transition region displayed in Fig. 1 covers a wide range of Ga, underlining the current uncertainty on the path instability threshold. This is partly due to the influence of the setup and to experimental uncertainties in the detection of the incipient instability [15]. However, the key issue is often the presence of surfactants that may affect the gas-liquid interface, changing the shear-free boundary condition satisfied by the liquid into a no-slip one at least on a part of the interface, therefore modifying the flow structure past the bubble, hence the threshold of the instability [16,17]. This is especially true with water, which is a polar liquid, and it is only during the past two decades that experiments could be carried out in ultrapure water where the shear-free condition is properly achieved [14].

The critical curve was also numerically determined in order to get rid of experimental issues and explore in more detail the connection between the evolution of the wake structure and the onset of the instability. The initial model used in the computational approach was that of an oblate spheroidal bubble with a prescribed aspect ratio (the length ratio of the major to minor axes, hereinafter denoted by χ). The direct numerical simulation (DNS) and linear stability analysis (LSA) approaches were applied to this simplified geometry, with the bubble maintained fixed in a uniform stream [18–20] or allowed to freely translate and rotate under the action of the buoyancy force [21,22]. However, under

real conditions, millimeter-size bubbles with a given volume do not exhibit a strict fore-aft symmetric shape: Compared to an oblate spheroid with the same aspect ratio, their front is somewhat flatter and their rear part is more rounded, owing to viscous effects [9,14]. This motivated more refined studies that considered realistic fore-aft asymmetric shapes. In this framework, axisymmetric DNS was employed in a first step to determine both the true axisymmetric bubble shape and the rise velocity just before the transition. With these characteristics known, path instability was studied either using three-dimensional DNS about the previously computed axisymmetric bubble shape [23] (solid line in Fig. 1) or again within the framework of LSA [24]. In the latter case, the bubble was again considered either fixed in a uniform stream (dashed line in Fig. 1) or freely moving (dash-dotted line), its rise velocity being set to the value provided by the axisymmetric DNS.

The two aforementioned studies undoubtedly improved over those in which a strictly oblate spheroidal shape was prescribed. However, they still prevent any further change in the bubble geometry as the instability develops. Although this assumption might be tenable when the Bond number is low, pressure fluctuations may easily alter the details of the bubble geometry when it is of $O(1)$ or larger. Under such conditions, a close coupling between the slight changes in the flow past the bubble and those of its shape is to be expected. Current LSA approaches also suffer from another restriction when the critical Galilei number becomes large, which is the case in pure water: When the bubble starts from rest under such conditions, it almost reaches its terminal velocity well before vorticity has fully diffused about it, owing to the large viscous time scale $\rho D^2/\mu$. Hence the base flow on which the disturbances that eventually yield path instability develop may not be strictly stationary, unlike what is assumed in LSA. These two reasons may explain in good part the discrepancies observed in Fig. 1 between experimental results and critical curves obtained from DNS and LSA, respectively.

Besides the quest for an accurate critical curve, significant effort has been devoted over the past 15 years, both experimentally and computationally, to determine how the wake past the bubble evolves with the style of path and how the coupling between the two operates. Indeed, starting from an axisymmetric structure when the bubble rises in straight line, the transition to a zigzagging path has been shown to be associated with the occurrence of a pair of counterrotating streamwise vortices preserving a symmetry plane, as observed in DNS [21,25] and experiments performed in ultrapure water [26] and silicon oils [10]. The wake past spiraling bubbles with a frozen oblate shape was also considered in Refs. [21,25], where it was found to be made of a pair of intertwined counterrotating vortices resulting in a frozen structure in the reference frame rotating with the bubble. Some more recent DNS studies examined the wake evolution during the rise of a freely deforming bubble, mostly in the zigzagging regime under conditions where time-dependent deformations remain modest [27,28] or in the wobbling regime where the shape exhibits large capillary-driven oscillations [29]. However, none of these studies focused on conditions close to the path instability threshold. Hence little is currently known regarding the influence of transient bubble deformations on the wake structure in the transitional regime.

Considering the state of the art summarized above, the aim of this study is to obtain a detailed description of the path and wake of a series of freely deforming rising bubbles with Bond and Galilei numbers corresponding to the region located in between and around the two critical curves of Fig. 1. By so doing, we seek to improve the determination of the actual critical curve of real bubbles and get insight into the intimate couplings between the path geometry, wake structure, and shape evolution.

The paper is organized as follows. First the numerical method and its validation are described in Sec. II, followed by an overview of the configurations considered in the computations. The central section of the paper is Sec. III, in which we discuss in detail the numerically observed paths and wakes and their couplings. In Sec. IV we examine the evolution of the rising speed in the various regimes and clarify the underlying mechanisms responsible for its characteristics. In Sec. V we review the various transitions identified in the simulations and their main characteristics and compare the present findings with state-of-the-art experimental and computational results to identify the current consensus and dissensus regarding the path instability threshold. Section VI provides a summary of the main findings of this study and suggests some avenues for future research.

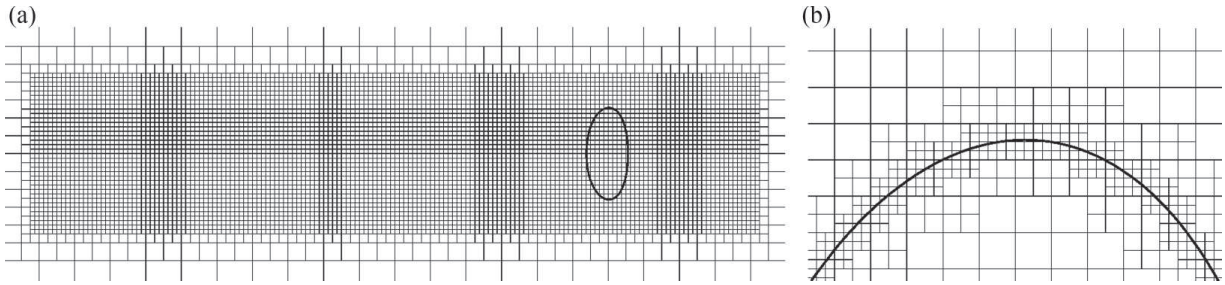

FIG. 2. Detail of a typical grid in the vicinity of the bubble: (a) refined region in the vicinity of the bubble, especially in the wake region (the last refinement level of the actual grid has been omitted in the figure to improve readability), and (b) refinement on both sides of the bubble surface.

II. NUMERICAL METHOD, VALIDATION, AND OVERVIEW OF THE SIMULATIONS

A. Numerical technique and grid characteristics

The results to be discussed below were generated by solving the three-dimensional, time-dependent Navier-Stokes equations in the entire gas-liquid domain. For this purpose, a one-fluid formulation based on the volume of fluid approach was employed, considering gas-to-liquid density and viscosity ratios of 10^{-3} and 10^{-2}, respectively. The numerical simulations were performed with the GERRIS flow solver open software [30]. The equations implemented in the solver are described in detail in Ref. [31] and will not be repeated here. Furthermore, the discretization techniques and additional computational details about the GERRIS code can be found in Refs. [30,32], which also provide several validation cases.

The three-dimensional domain has a horizontal cross section of $8D \times 8D$ and is $128D$ high in order to allow the bubble motion to be tracked over a long time. This domain is discretized in cubic finite volumes, hierarchically organized as an octree, which allows for a concentration of grid cells at the interface and in the wake region, by refining a region of $2D \times 2D \times 10D$ around the bubble and in the near wake. When dealing with bubbles exhibiting large lateral displacements, we expand the size of the refined region to $4D \times 4D \times 20 \sim 30D$, depending on the spatial decay of the wake. The spatial resolution is the same as the one employed in Ref. [31], where a detailed comparison between axisymmetric and fully-three-dimensional simulations was carried out and showed good agreement (for a typical case, the terminal velocity and aspect ratio provided by the two approaches were found to differ by less than 1.5% and 0.8%, respectively). This comparative analysis was used afterward to validate the configuration, domain size, grid density, and boundary conditions employed in the present study. At the interface (in the wake), the grid has a density of 128 (32) cells per bubble equivalent diameter (this corresponds to the level 4 of refinement in the terminology of [23]); a typical example of the grid around and within the bubble is displayed in Fig. 2. A no-slip boundary condition is applied at the bottom and on the vertical lateral walls of the domain, while an outflow condition is prescribed at the top. Computations are initiated with a spherical bubble shape, as in Refs. [23,31], with the bubble center initially standing $3D$ above the bottom wall. No disturbance is added to trigger the instability. Hence the latter occurs solely due to the propagation of truncation and roundoff errors. It is worth pointing out that these computations have a high computational cost, owing to the large number of grid cells [$O(10^7)$] required to resolve the boundary layer and wake consistently and the large number of time steps [$O(2.5 \times 10^5)$] required to follow the bubble during a long time and capture the possible late transitions of its path and wake.

B. Validation

The accuracy of the computational predictions in the axisymmetric flow regime was discussed in detail in Ref. [23]. It was shown, for instance, that in the case of a marginally stable configuration corresponding to a bubble with $\mathrm{Ga} = 239$ and $\mathrm{Bo} = 0.44$ rising in pure water, computational

predictions differ from experimental observations [14] by 0.17% for the terminal velocity and 3.5% for the aspect ratio, respectively. However, this comparison was limited to quantities characterizing the final steady state. Since we are concerned with possible transient changes in the bubble shape, we also wished to check that capillary-driven oscillations are properly captured with the grid resolution defined above. For this purpose we ran a specific series of three-dimensional computations in which we tracked the evolution of bubbles released from rest with a slightly nonspherical shape. We considered both fixed (i.e., nonrising) and rising bubbles characterized by a local pole-to-pole initial radius $2r(\theta,t^*=0)/D = 1+\epsilon P_n(\theta)$, where $P_n(\theta)$ is the Legendre polynomial associated with the axisymmetric oscillation mode of order n, ϵ is the dimensionless amplitude of the initial deformation, and θ denotes the polar angle (throughout the paper, t^* denotes a dimensional time). In the classical viscous potential flow approximation, linear axisymmetric oscillations of mode n of a fixed, almost spherical bubble are known to evolve as $e^{[i\omega(n)-\tau^{-1}(n)]t^*}$, where the radian frequency and characteristic damping time are respectively given by [33]

$$\omega^2(n) = 8(n-1)(n+1)(n+2)\frac{\sigma}{\rho D^3}, \quad \tau(n) = \frac{1}{4(n+2)(2n+1)}\frac{D^2}{\nu}. \tag{1}$$

The leading-order finite-Reynolds-number corrections to (1) resulting from the shear-free boundary condition at the bubble surface respectively scale as $\mathrm{Re}_{\mathrm{osc}}^{-3/2}$ and $\mathrm{Re}_{\mathrm{osc}}^{-1/2}$ [34], with $\mathrm{Re}_{\mathrm{osc}} = \sqrt{\rho\sigma D}/\mu$, so that (1) holds for large enough $\mathrm{Re}_{\mathrm{osc}}$. We ran computations for bubbles with an initial slightly prolate shape corresponding to $\epsilon = 0.075$ so as to ensure that oscillations stay in the linear regime. We extracted the evolution of the bubble shape, expanded it in the form $2r(\theta,t^*)/D = 1+\sum a_n(t^*)P_n(\theta)$ and determined the optimal fit to the evolution of the amplitude of mode $n=2$, i.e., $a_2(t^*)$, by an exponentially damped cosine function. This allowed us to conclude that, with the grid used throughout this work, $\omega(2)$ and $\tau(2)$ are predicted with an accuracy of the order of 1%–2%. For instance, with $\mathrm{Re}_{\mathrm{osc}} = 70.7$, we found that predictions differ from (1) by 1.8%, in both the frequency and damping time.

The case of rising bubbles is more complex because capillary deformations generally develop on a nonspherical time-evolving surface. Then spherical harmonics are not eigenfunctions of the linear dynamical problem anymore. Hence, starting with the above form of $r(\theta,t^*=0)$, modes of order m with $m \neq n$ subsequently develop. Moreover, one has to distinguish between axisymmetric modes [with, for mode (2,0) in the nomenclature of spherical harmonics, two wavelengths along the perimeter of the vertical bubble cross section] and nonaxisymmetric ones [with, for mode (2,2), two wavelengths along the bubble equator]. In the case of an oblate spheroid with a prescribed aspect ratio, the frequency of the first oscillation modes was computed in the inviscid limit as a function of the oblateness in Ref. [35] and was shown to be a slowly decreasing function of χ. We computed the evolution of a bubble corresponding to $\mathrm{Bo} = 2.36$ and $\mathrm{Ga} = 108.6$ (i.e., $\mathrm{Re}_{\mathrm{osc}} = 70.7$ since $\mathrm{Re}_{\mathrm{osc}} = \mathrm{GaBo}^{-1/2}$), which, according to Fig. 1, falls within the transition region. Again, a slightly prolate initial shape with $\epsilon = 0.075$ was selected. The evolution of the bubble aspect ratio is displayed in Fig. 3(a). The final aspect ratio χ_T is 1.89, whereas the final Reynolds number Re_T is 145. Both predictions compare very well with those recently obtained with a level-set approach on a uniform three-dimensional grid with 48 cells per bubble diameter [36], namely, $\chi_T = 1.91$ and $\mathrm{Re}_T = 142$. To evaluate how the characteristics of the oscillations evolve in such a configuration, effects of the variation of the mean bubble shape must be removed [37]. We achieved this by considering a succession of time windows and separating the time-averaged and time-dependent contributions to the amplitude of mode (2,0) in each of them. The radian frequency of this mode within each window $\omega(2,0)$ could then be determined, together with the corresponding time-averaged aspect ratio $\langle\chi\rangle$. The resulting variation of $\omega(2,0)$ is plotted against $\langle\chi\rangle$ in Fig. 3(b). Although the rapid damping of the oscillations lowers the accuracy of the procedure as $\langle\chi\rangle$ increases, resulting in a non-negligible scatter, the general tendency is found to follow the theoretical inviscid prediction [35].

All numerical tests reported in the literature aimed at reproducing the characteristics of planar capillary waves or drop or bubble oscillations were performed on two-dimensional or axisymmetric

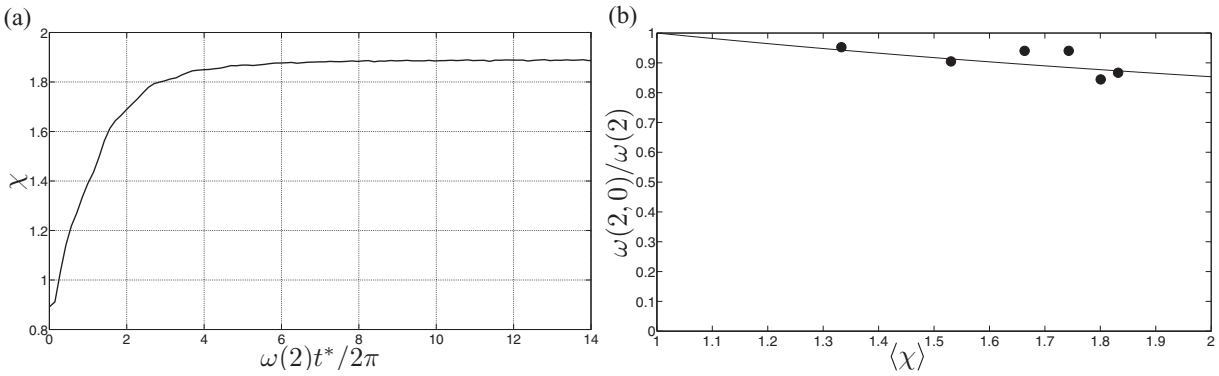

FIG. 3. Rise of an initially slightly prolate bubble corresponding to Bo = 2.36 and Ga = 108.6: (a) evolution of the aspect ratio and (b) variation of the frequency of mode (2,0) with the time-averaged aspect ratio. In (b) the solid line corresponds to the inviscid prediction of [35].

grids. Discretizing an axisymmetric shape on a three-dimensional Cartesian grid unavoidably introduces additional numerical errors because the grid does not fit with the surface in the azimuthal direction. This is why the accuracy of the predictions obtained in the tests reported above makes us confident that the grid used throughout this work is suitable to properly capture time-dependent deformations of the bubble surface in the transition regime on which we focus.

C. Overview of the simulations

Figure 4 shows the position in the (Bo,Ga) plane of the various bubbles analyzed in this work. Twenty-six bubbles, all located in the neighborhood of the transition curves determined in Refs. [23,24], were considered. We selected five values of the Morton number (see Table I) and varied the Bond and Galilei numbers along each iso-Mo line by properly modifying the fluid properties, following the procedure described in Ref. [24]. The selected values of Mo correspond to ultrapure water at a temperature of 28 °C (Mo = 1.11×10^{-11}) and different silicon oils at a temperature of 22 °C, which were respectively employed in Refs. [9,26] to study the transition from an experimental point of view. Table I also indicates the value of the Bond and Galilei numbers, the style of path and wake

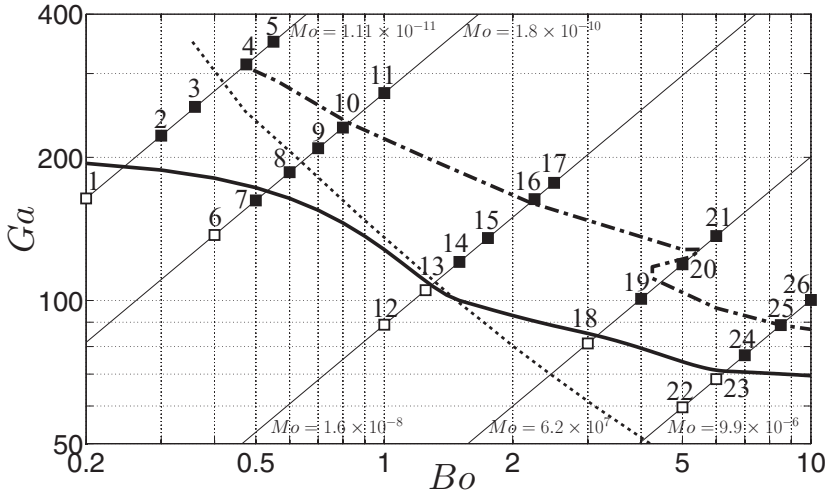

FIG. 4. Phase diagram showing the entire set of simulations and positioning them in the (Bo,Ga) plane with respect to the two neutral curves displayed in Fig. 1. Open (closed) symbols refer to runs in which the rectilinear bubble path was found to be stable (unstable). The dotted line represents the critical curve beyond which a standing eddy exists [23] and the thin solid lines correspond to iso-Mo lines (shown from left to right are water at 28 °C and silicon oils T00, T02, T05, and T11, respectively, all at a temperature of 22 °C). The various bubbles are numbered as in Table I.

TABLE I. Characteristic properties of the 26 flow conditions considered in this study. Here 2CRV, SHV, and FS stand for two counterrotating vortices, secondary hairpin vortices, and flattened spiraling, respectively; following the terminology of [38], the terms 2R and 4R refer to the number of vortex loops per period in the wake of zigzagging bubbles.

Case	Liquid	Mo	Bo	Ga	St	Path	Wake	Regime
1	water	1.11×10^{-11}	0.2	163.88		rectilinear	axisymmetric	rectilinear
2	water	1.11×10^{-11}	0.3	222.13		chaotic	2CRV aperiodic	chaotic
3	water	1.11×10^{-11}	0.36	255.28		chaotic	2CRV aperiodic	chaotic
4	water	1.11×10^{-11}	0.475	313.54	0.042	chaotic or elliptical spiral	2CRV aperiodic+SHV	transitional
5	water	1.11×10^{-11}	0.55	350.20	0.045	elliptical spiral → planar zigzag	2CRV 2R+SHV	FS → zigzagging
6	T00	1.8×10^{-10}	0.4	137.31		rectilinear	axisymmetric	rectilinear
7	T00	1.8×10^{-10}	0.5	162.34		chaotic	2CRV aperiodic	chaotic
8	T00	1.8×10^{-10}	0.6	186.12		chaotic	2CRV aperiodic	chaotic
9	T00	1.8×10^{-10}	0.7	208.93		chaotic	2CRV aperiodic	chaotic
10	T00	1.8×10^{-10}	0.8	230.94	0.054	planar zigzag	2CRV+SHV	zigzagging
11	T00	1.8×10^{-10}	1.0	273.01	0.060	elliptical spiral → planar zigzag	2CRV+SHV	FS → zigzagging
12	T02	1.6×10^{-8}	1.0	88.92		rectilinear	axisymmetric	rectilinear
13	T02	1.6×10^{-8}	1.25	105.11		rectilinear	axisymmetric	rectilinear
14	T02	1.6×10^{-8}	1.50	120.51	0.069	planar zigzag	2CRV 2R	zigzagging
15	T02	1.6×10^{-8}	1.75	135.3	0.073	planar zigzag	2CRV 2R	zigzagging
16	T02	1.6×10^{-8}	2.25	163.35	0.090	elliptical spiral → planar zigzag	2CRV 4R	FS → zigzagging
17	T02	1.6×10^{-8}	2.5	176.77	0.095	elliptical spiral → planar zigzag	2CRV 4R	FS → zigzagging
18	T05	6.2×10^{-7}	3.0	81.23		rectilinear	axisymmetric	rectilinear
19	T05	6.2×10^{-7}	4.0	100.8	0.108	planar zigzag	2CRV 2R	zigzagging
20	T05	6.2×10^{-7}	5.0	119.2	0.123	planar zigzag	2CRV 4R	zigzagging
21	T05	6.2×10^{-7}	6.0	136.6	0.138	elliptical spiral → planar zigzag	2CRV 4R	FS → zigzagging
22	T11	9.9×10^{-6}	5.0	59.61		rectilinear	axisymmetric	rectilinear
23	T11	9.9×10^{-6}	6.0	68.34		rectilinear	axisymmetric	rectilinear
24	T11	9.9×10^{-6}	7.0	76.72	0.120	planar zigzag	2CRV 2R	zigzagging
25	T11	9.9×10^{-6}	8.5	88.74	0.132	planar zigzag	2CRV 2R	zigzagging
26	T11	9.9×10^{-6}	10.0	100.25	0.136 → 0.174	planar zigzag → helix (spiral)	spiral	spiraling

structure (or the succession of them) identified during the bubble ascent, and, when appropriate, the Strouhal number $\mathrm{St} = fD/U_T$, where f is the oscillation frequency of the path and U_T is the bubble terminal velocity. In the figures displayed in the next section, all variables are made dimensionless using the equivalent diameter D and the gravitational time $\sqrt{D/g}$ as characteristic length and time scales, respectively. The only exception is the vorticity, which is normalized using the characteristic time scale D/U_T. Thus, the main features of the vortical structures that develop in the wake are discussed using isocontours of the dimensionless streamwise vorticity $\omega_x = \partial w/\partial y - \partial v/\partial z$, where x (u) is the dimensionless vertical coordinate (velocity) and y and z (v and w) lie in a horizontal plane.

III. OBSERVED SHAPES, PATHS, AND WAKES

In this section we comment on the key results of this study, focusing on the observed paths, wake structures, and interface shapes for a representative sample of the 26 bubbles that were considered.

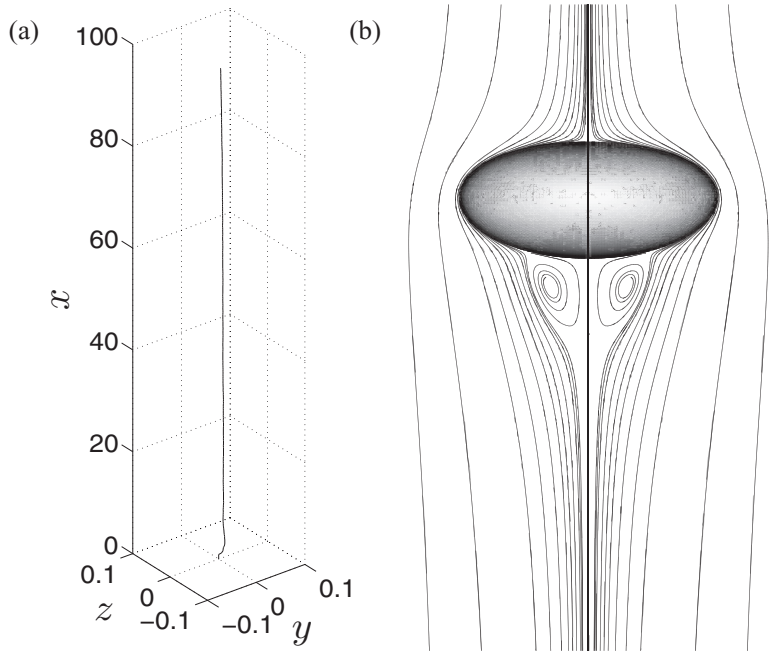

FIG. 5. (a) Three-dimensional reconstruction of the path followed by bubble number 22 in Table I. (b) Streamlines of the flow around the bubble showing its axisymmetry and the presence of a standing eddy.

Emphasis is put on the discussion of the underlying mechanisms in order to identify the causes or the nature of several puzzling behaviors. The five dynamical regimes we observed during the computations are not presented in ascending order of the Bond and Galilei numbers. Rather, we start by commenting on the three already-well-identified regimes, namely, vertical axisymmetric, planar zigzagging, and helical or spiraling, before discussing the more complex flattened spiraling regime and the chaotic regime revealed by these simulations.

A. Rectilinear regime

When the Bond and Galilei numbers are below the lowest critical curve reported in Fig. 4, bubbles rise following a straight vertical trajectory and the flow field around them is axisymmetric as can be observed, for example, in Fig. 5 for bubble number 22 in Table I; the same behavior was found for bubbles 1, 6, 12, 13, 18, 22, and 23. In this stable regime, once the bubbles reach their terminal velocity, they rise while keeping their shape unaltered. Additionally, Fig. 5(b) shows the streamlines around the bubble, confirming that the flow is axisymmetric with a toroidal vortex attached to the rear part of the bubble. However, displaying the streamlines corresponding to the flow field around bubble number 12, for instance, would reveal that no such attached vortex exists in this case. This is consistent with the position of the dotted line in Fig. 4, which corresponds to the critical conditions for the existence of a standing eddy. Indeed, such eddies result from an accumulation of vorticity at the back of the bubble [39] and the vorticity generated on a surface on which the flow obeys a shear-free condition is known to be proportional to the product of the surface curvature by the tangential fluid velocity [40]; hence only bubbles with an aspect ratio exceeding a threshold value that depends on the rise Reynolds number exhibit an attached toroidal vortex [41]. Small initial deviations in the path may be noticed in Fig. 5(a). They result from the cumulated effects of several potential sources of tiny asymmetries, such as off-centering of the initial bubble position within the three-dimensional grid, departures from axisymmetry of its initial shape, and asymmetries of truncation errors. These errors tend to trigger the instability of the bubble path. In the present case, the system quickly develops an axisymmetric behavior, which allows us to conclude that it is stable with respect to infinitesimal disturbances.

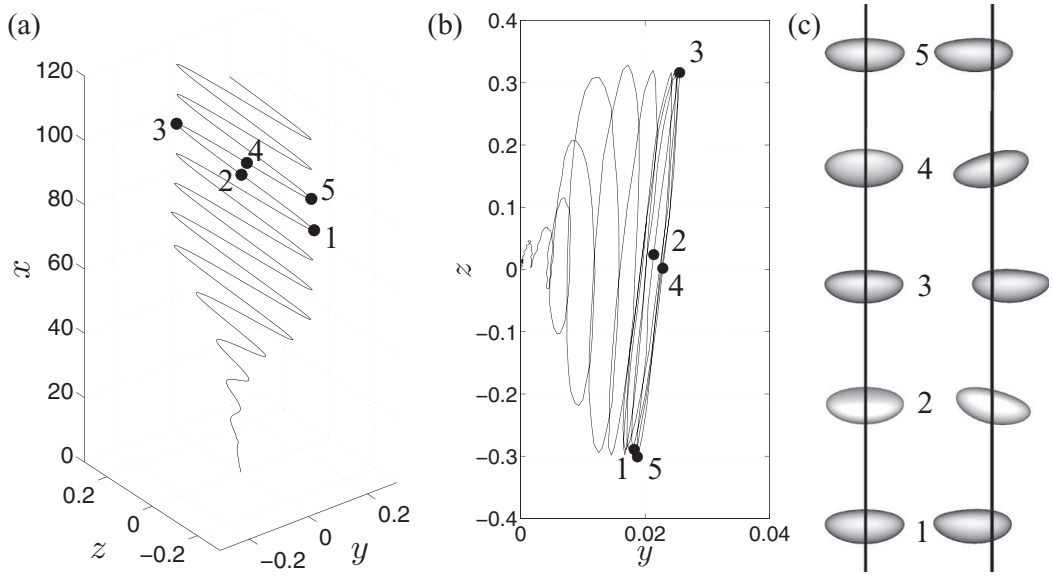

FIG. 6. (a) Three-dimensional reconstruction and (b) top view of a bubble trajectory typical from the zigzagging regime (bubble number 19 in Table I). (c) Two perpendicular views of the temporal evolution of the bubble shape at positions indicated by bullets in (a) and (b); the solid line corresponds to the average vertical (x) axis of the path.

B. Planar zigzagging regime

The zigzagging motion of a rising or falling body is characterized by a constant periodic lateral drift from one side to the other taking place within a plane. Such characteristics can be observed in Fig. 6(a), where a three-dimensional view of the bubble path in this regime is plotted. Here, with bubble number 19, the amplitude of the lateral drift is about $\pm 0.3D$ and the maximum inclination with respect to the vertical, say, ψ_0, is about 14°. These findings are in excellent agreement with the observations reported in Ref. [10] with the same (Bo,Ga) pair. As shown in Fig. 6(b), the path is not strictly planar in its early stages, its cumulated drift in the (y,z) plane being of $O(10^{-2}D)$. Nevertheless, this drift decreases over time and, after path instability has saturated, the bubble goes on zigzagging in a plane. Since no perturbation is added to trigger the instability, the selection of this plane entirely results from the various sources of error listed above. The right sequence in Fig. 6(c) indicates that the minor axis of the bubble is vertical at positions 1, 3, and 5, which correspond to the maximal lateral excursion, i.e., there is no inclination of the bubble with respect to its path. Starting from position 1 or 3, the bubble begins to tilt toward the direction of the path, achieving its maximum inclination in the middle of the next branch of the zigzag, i.e., at position 2 or 4. In the second half of this branch, this inclination reduces until it vanishes again at the next extremity, i.e., at position 3 or 5. All along the zigzags, the bubble minor axis remains virtually aligned with the local direction of the path. This is actually a general characteristic of the zigzagging motion of axisymmetric bodies with aspect ratios not too far from unity [6,42], in contrast to the behavior of flat bodies. The left sequence in Fig. 6(c) shows that, once in the fully developed zigzagging regime, the bubble cross section perpendicular to the plane of the zigzag remains constant (the projected area is seen to vary somewhat over time, but this variation is entirely due to the varying bubble inclination). In contrast, the right sequence reveals that the bubble is more pointed (i.e., it has a larger maximum curvature) on its left at positions 1 and 5 and on its right at position 3. This is an indication that some deformation is going on within the plane of the zigzag. More precisely, the corresponding maximum curvature is seen to be larger (smaller) at the exterior (interior) of the zigzag. This trend is readily rationalized by noting that the bubble rotates about its major axis perpendicular to the plane of its path and the corresponding rotation rate is maximum at the extremities of the zigzag. Hence, in the reference frame moving with the bubble centroid, the local tangential fluid velocity is larger (smaller) at the exterior (interior) of the zigzag. This results

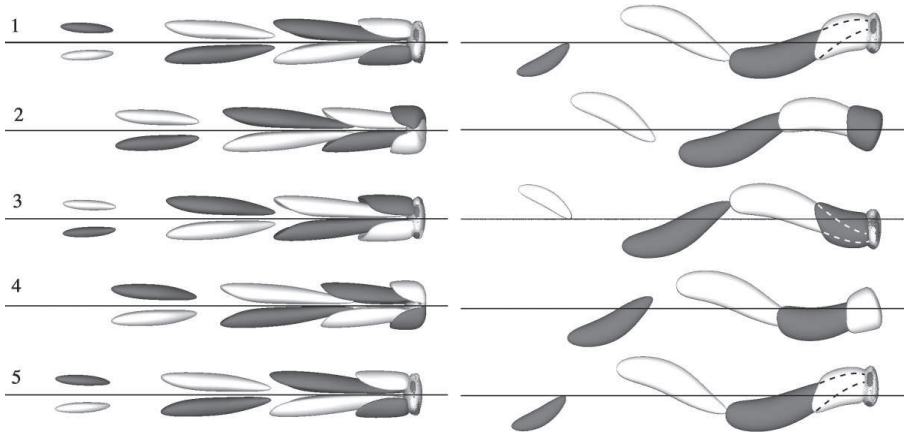

FIG. 7. Evolution of the streamwise vorticity isocontours $\omega_x = \pm 0.24$ at five successive positions corresponding to the bullets shown in Figs. 6(a) and 6(b) for bubble number 19. The left and right panels correspond to two perpendicular views. In the right panel, the dotted lines mark the hidden part of the primary isocontour at positions 1, 3, and 5.

in a lower (higher) local pressure, making the bubble deform more on the side located the farthest away from the zigzag centerline. This effect can be quantified by considering that the inclination of the bubble minor axis obeys the law $\psi(t^*) = \psi_0 \cos(2\pi f t^*)$. Thus, when the bubble reaches an extremity of the zigzag, its rotation rate is $2\pi f \psi_0$ and the difference in the fluid velocity at the two points located at the intersection of its equator and the plane of its path is $\Delta U = 2\pi f D \psi_0 g(\chi)$, where $g(\chi)$ may be estimated from the irrotational prediction for the flow induced by the rotation of an oblate spheroid [33], i.e., $g(\chi) = \chi^{1/3}(\chi^2 - 1)[\sec^{-1}\chi - (2\chi^2 + 1)(\chi^2 - 1)^{1/2}/3\chi^2][(\chi^2 + 1)\sec^{-1}\chi - 2(\chi^2 - 1)^{1/2} - (\chi^2 - 1)^{3/2}/3\chi^2]^{-1}$. On the equator, the rise of the bubble yields an average vertical fluid velocity $h(\chi)U_T$, with, again from potential flow theory [33], $h(\chi) = (\chi^2 - 1)^{3/2}[\chi^2 \sec^{-1}\chi - (\chi^2 - 1)^{1/2}]^{-1}$. Therefore, the pressure difference resulting from the velocity difference ΔU is $\Delta P \approx \rho h(\chi) U_T \Delta U$, which is to be compared with the mean pressure difference $\Delta P_{\text{av}} = \rho[h(\chi)U_T]^2/2$ between the front stagnation point and the equator. Hence $\Delta P/\Delta P_{\text{av}} \approx 2\Delta U/h(\chi)U_T \approx 4\pi\, \text{St}\psi_0 g(\chi)/h(\chi)$. For bubble number 19 we have $\text{St} = 0.108$, $\psi_0 = 14^\circ$, and $\chi \approx 2.11$ [hence $g(\chi) \approx 0.80$ and $h(\chi) \approx 2.18$], so $\Delta P/\Delta P_{\text{av}} \approx 0.12$. Although one order of magnitude smaller than the deformation resulting from ΔP_{av}, it is likely that the pressure difference ΔP induces a significantly nonuniform distribution of the curvature of the bubble surface within the equatorial plane, provided the Bond number is at least of $O(1)$, and this is indeed what is seen in Fig. 6(c).

The zigzagging regime is characterized by a wake structure consisting of two counterrotating trailing vortices exhibiting a symmetry plane, as can be appreciated in Fig. 7. The sign of the trailing vorticity within each thread changes every half-period of the zigzag. However, as shown in Ref. [25], this change does not coincide with the inflection point of the path, or with the maximum lateral excursion of the bubble, rather being located in between the two. This is confirmed by Fig. 7, which shows that the primary vortex pair changes its sign in between points 1 and 2 (2 and 3) during the first (second) half-cycle. This mode was experimentally observed in Refs. [10,43], as well as in DNS [21]. Looking at the various bubbles in Table I for which a planar zigzagging regime was encountered, it may be noticed that the frequency of the periodic motion increases significantly with the Bond number, i.e., the length of the isovorticity contours in each thread, such as those shown in Fig. 7, decreases. Indeed, the Strouhal number ranges from 0.054 for $\text{Bo} = 0.8$ to 0.132 for $\text{Bo} = 8.5$. Actually, the Morton number also changes from one case to another, so there may be some influence of the viscosity as well. Nevertheless, Mo keeps the same value for bubbles 24 and 25. Since the former corresponds to $\text{Bo} = 7.0$ and has $\text{St} = 0.120$ while the latter corresponds to $\text{Bo} = 8.5$ and has $\text{St} = 0.132$, the dominant influence of the Bond number is clear. Although not reported in Table I, the amplitude of the bubble lateral shift is also found to increase significantly

FIG. 8. Two perpendicular views of the wake structure in the zigzagging regime revealed by the λ_2 criterion (bubble number 19). The bubble is visible on the right.

with the Bond number: For instance, with $\mathrm{Mo} = 1.6 \times 10^{-8}$, the crest-to-crest amplitude is found to vary from $0.8D$ for bubble 15 ($\mathrm{Bo} = 1.75$) to $1.35D$ for bubble 17 ($\mathrm{Bo} = 2.5$).

The vortical structure in the wake is also displayed in Fig. 8 in two perpendicular planes, using the λ_2 criterion [44]. Not surprisingly, this structure is close to that observed in the wake of fixed or tethered axisymmetric bodies in the range of parameters in which they exhibit a periodic vortex shedding regime preserving a planar symmetry (e.g., a fixed solid sphere at a Reynolds number of 300 in Refs. [45,46] or fixed circular disks with aspect ratios in the range 5–10 and Reynolds numbers in the range 170–180 in Refs. [47,48]). However, the present wake reveals a key difference with respect to that of fixed bodies: In the latter case, the lift force, although oscillating, keeps a constant sign, so the wake is made of a single-sided chain of vortex loops [referred to as the R (ring) mode of vortex formation in Ref. [38]]. Here, in contrast, the averaged lift force over a full zigzag period is zero as the bubble mean path is vertical. As a consequence, in addition to its planar symmetry, the wake exhibits an averaged left-right symmetry and is made of a two-sided chain of vortex loops (the 2R mode according to the nomenclature of [38]) as the bottom view in Fig. 8 shows.

Although it may at first glance seem generic of the planar zigzagging regime, it turns out that the wake structure we just described is not. This can be appreciated by examining its counterpart in the final stage of the rise of bubble number 16. Over a long time, this bubble follows a flattened spiraling path that will be described in a forthcoming paragraph. However, this spiral flattens more and more as time proceeds, so the bubble eventually describes planar zigzags. The structure of the corresponding wake, revealed by the λ_2 criterion, is displayed in Fig. 9. As the top view in Fig. 9(a) shows, the

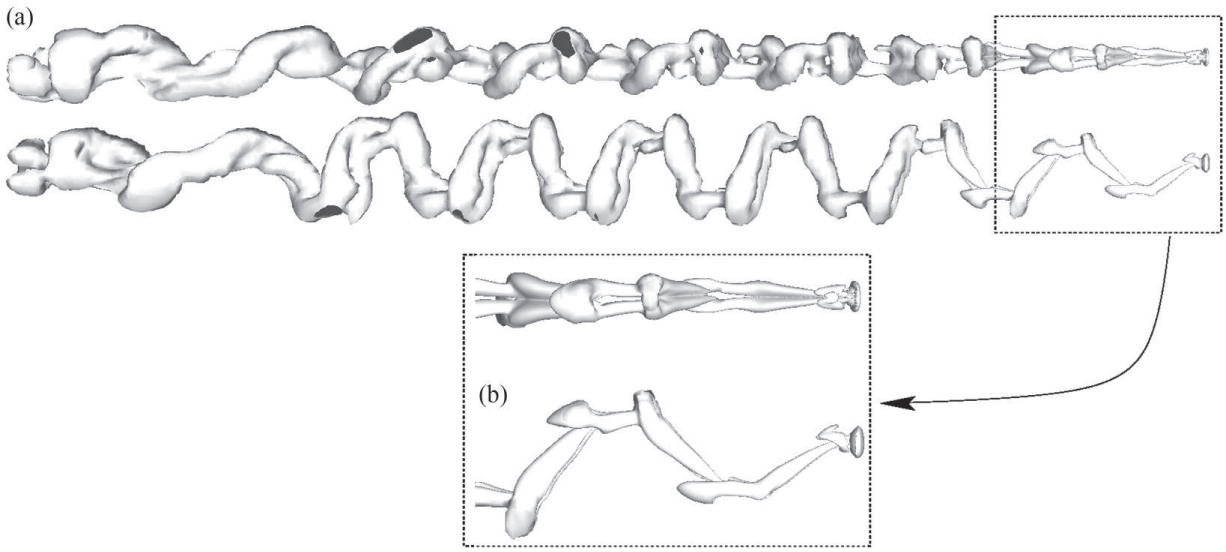

FIG. 9. Two perpendicular views of the wake structure revealed by the λ_2 criterion at the end of the rise of bubble number 16: (a) complete wake and (b) zoom-in of the near wake.

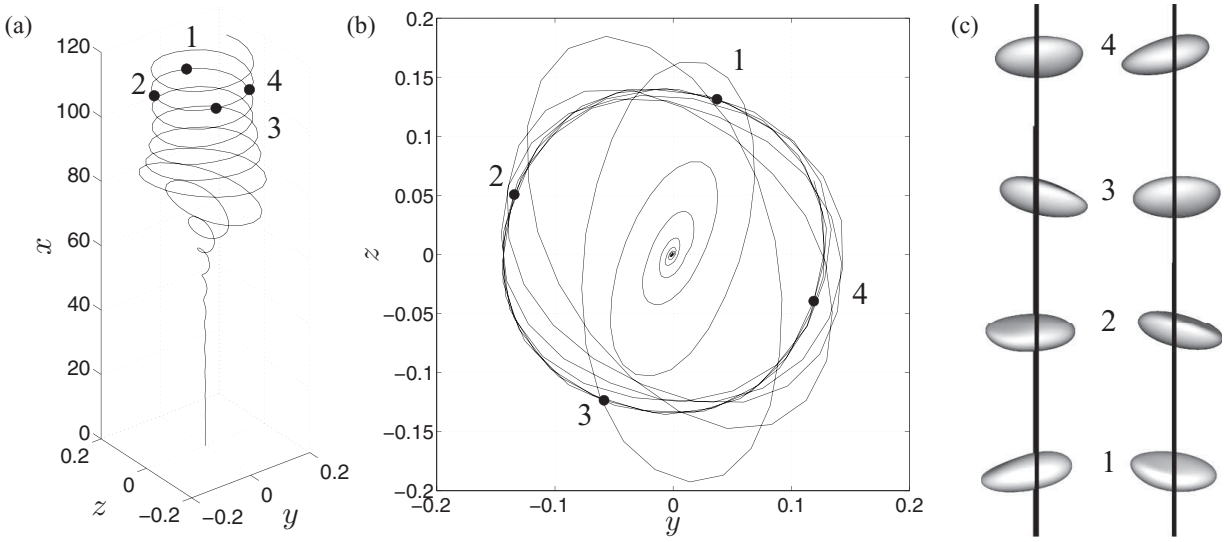

FIG. 10. (a) Three-dimensional reconstruction and (b) top view of the trajectory corresponding to bubble number 26. (c) Two perpendicular views of the temporal evolution of the bubble shape corresponding to the bullets in (a) and (b).

wake exhibits a symmetry plane only up to a position about $10D$ downstream of the bubble, whereas at larger distances the two threads become strongly intertwined, in line with the three-dimensional nature of the "old" path. Focusing on the near wake where a symmetry plane exists [Fig. 9(b)], the bottom view reveals that the previously described 2R mode is now replaced by a 4R mode in which a second single-sided loop superimposes onto the primary one. While the latter is generated every half-cycle of the zigzag near its extremities, the former emerges near the inflection point (i.e., the centerline) of the path. This mode was also identified and described in detail in Ref. [38] in the context of freely falling spheres. The authors showed that it is specific to zigzagging spheres and emerges in the form of a loop after the primary streamwise vortex pair has pinched off. Moreover, they were able to pinpoint that this pinch-off is induced by the small oscillations with frequency $2f$ of the body vertical velocity that take place in between two extremities of a zigzag with frequency f: Having suppressed artificially these oscillations, they recovered a 2R wake structure similar to that shown in Fig. 8. To check whether or not the same mechanism holds here, it is relevant to compare the evolutions of the rising speed, i.e., Reynolds number, for bubbles 19 and 16 in Figs. 20(c) and 20(e) (on which we will comment in more detail later). It turns out that the relative magnitude of the rising speed oscillations is typically five times larger for bubble 16, which gives additional credit to the connection suggested in Ref. [38]. Finally, it is worth noting that Fig. 9(a) suggests that the 4R mode is robust, as it subsists at least over $40D$ downstream of the bubble, although the wake has lost it planar symmetry long before.

C. Spiraling (helical) regime

For the highest value of the Morton number considered in this study, $\mathrm{Mo} = 9.9 \times 10^{-6}$, the largest bubble (number 26) describes a spiraling path, as can be seen in Figs. 10(a) and 10(b). More precisely, this bubble follows an elliptic spiraling path whose minor-to-major axes ratio increases over time, ending in a circle with a diameter about $0.28D$. Hence, once it has reached its terminal velocity, its final path is nothing but a circular helix. In line with our previous observations, the bubble shapes displayed in Fig. 10(c) exhibit a left-right asymmetry in their diametrical plane, being more pointed in the region looking toward the path exterior. This asymmetry is noticeable in this case since the Bond number is large ($\mathrm{Bo} = 10$), resulting in weak surface tension effects.

The corresponding wake structure is displayed using isocontours of the streamwise vorticity in Fig. 11. This structure is characterized by a pair of fully intertwined streamwise vortices. The

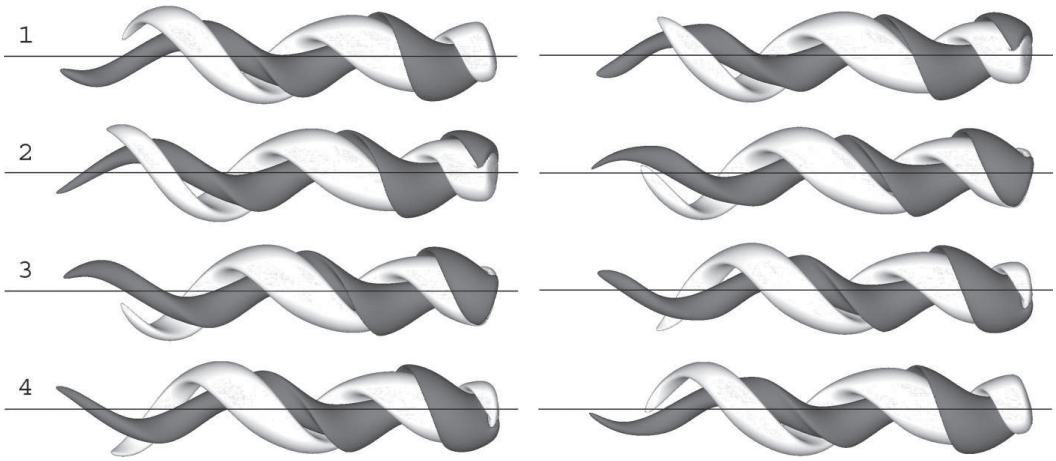

FIG. 11. Evolution of the streamwise vorticity isocontours $\omega_x = \pm 0.24$ at four successive positions corresponding to the bullets shown in Fig. 10 for bubble number 26. The left and right panels correspond to two perpendicular views.

two threads are totally disconnected, i.e., no hairpin is present, in contrast to the wake structure observed in the case of planar zigzags. They wrap up around one another, yielding a double spiral (or corkscrew) wake structure. This is in line with the DNS observations reported in Refs. [21,25] at much higher Reynolds number (Re $\approx$ 600 instead of 80 in the present case); in the latter reference it was shown that this wake looks frozen when observed in a reference frame attached to the bubble and delivers a constant force and torque on it. Not unlikely, the vortical structures characteristic of this spiraling regime are similar to those observed elsewhere in the wake of spinning solid bodies, a context in which they were referred to as spiral modes [49,50].

D. Flattened spiraling regime

For the lowest four values of the Morton number considered in this study, a flattened spiraling regime with an approximately elliptical horizontal projection was observed at the highest values of Ga in each series. In general, this regime appears to be a more or less long transient that eventually converges either toward a planar zigzagging regime when the ellipse flattens gradually (this is the case with bubbles 5, 11, 16, 17, and 21) or toward a helical regime when it tends toward a circle, as previously seen with bubble number 26. However, this transient may be very long, maintaining the path geometry in between those of a planar zigzag and a circular helix over a vertical distance of $O(10^2 D)$ as may be observed in the two examples discussed below. Thus, it is no surprise that in many experiments (and computations) performed in devices of limited height, this intermediate three-dimensional regime has been considered as a stable state. It may be thought of as resulting from the continuous (but generally nonuniform) precession of a planar zigzag. Two typical paths corresponding to this regime are displayed in Figs. 12(a), 12(b), 13(a), and 13(b) for bubbles number 5 and 16, respectively. Qualitatively similar behaviors have been noticed in several experiments, especially those performed in ultrapure water in Ref. [51]. However, it must be stressed that these experiments were performed at significantly higher Reynolds number ($\mathrm{Re}_T \geqslant 10^3$), so the observed flattened spiraling paths *succeed* the planar zigzagging or helical paths when the bubble diameter is increased and announce the transition to the high-Reynolds-number chaotic (rocking) motion, whereas here they *precede* the occurrence of the well-defined planar zigzagging and spiraling regimes.

The two elliptical spirals shown in Figs. 12(a), 12(b), 13(a), and 13(b) converge towards a planar zigzag, as the wake structure displayed in Fig. 9 shows in the latter case. The evolution of the bubble shape plotted in Figs. 12(c) and 13(c) reveals departures from axisymmetry [see, for instance, snapshot 3 (2) in the left column of the former (latter) figure]. Again, this left-right asymmetry is due to the bubble rotation. It is not unlikely that it is especially visible at the positions mentioned above,

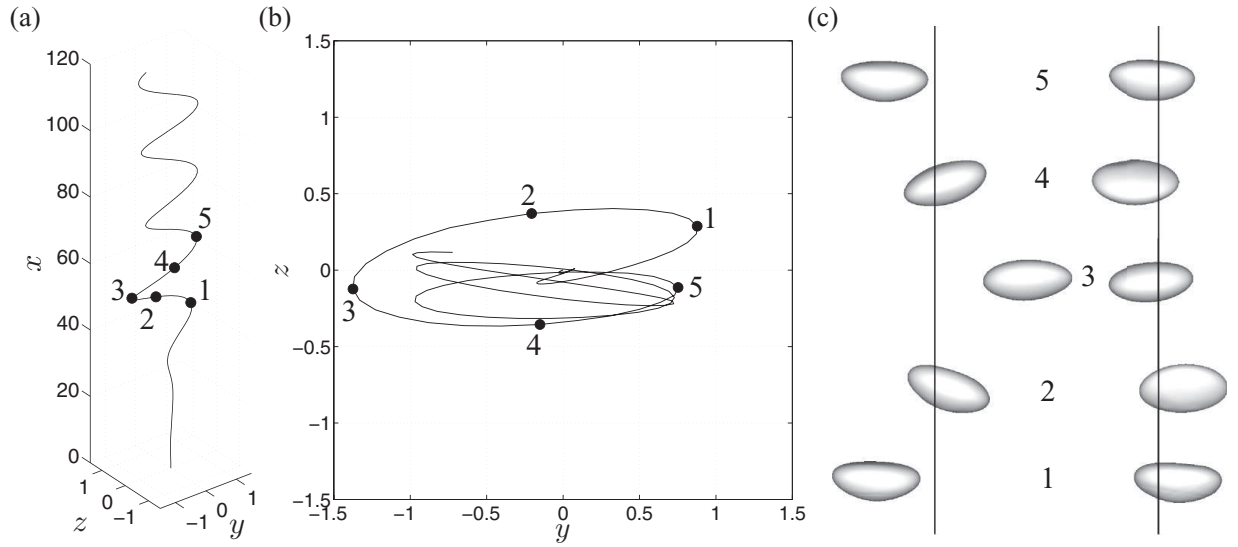

FIG. 12. (a) Three-dimensional reconstruction and (b) top view of a bubble trajectory typical from the flattened spiraling regime (bubble number 5). (c) Two perpendicular views (on the left, the x-z plane and on the right, the x-y plane) of the evolution of the bubble shape corresponding to the bullets in (a) and (b).

which both correspond to the maximum lateral excursion of the bubble. However, this asymmetry is less salient for bubble 5, whose Bond number is four times smaller than that of bubble 16.

Figure 14 displays two perpendicular views of the wake evolution past bubble 5. The wake structure resembles that observed in the planar zigzagging regime, as it is still dominated by a pair of counterrotating streamwise vortices whose sign changes alternately. However, as could be expected, no symmetry plane can be seen in either of the two views. Rather, the two vorticity threads are slightly twisted around each other as evidenced in the right frame, a situation resulting in a nonzero axial torque on the bubble. Moreover, an additional spectacular feature is the presence of short-wavelength undulations of isovorticity contours, which start to develop some distance downstream of the bubble and progressively invade the far-wake structure. Figure 15 displays the topology of the same wake extracted with the help of the λ_2 criterion. As shown in this figure, the secondary vortices take the form of single-sided loops superimposed onto each primary vortex. One can identify approximately four such loops along each primary vortex, which makes the corresponding wake mode unambiguously

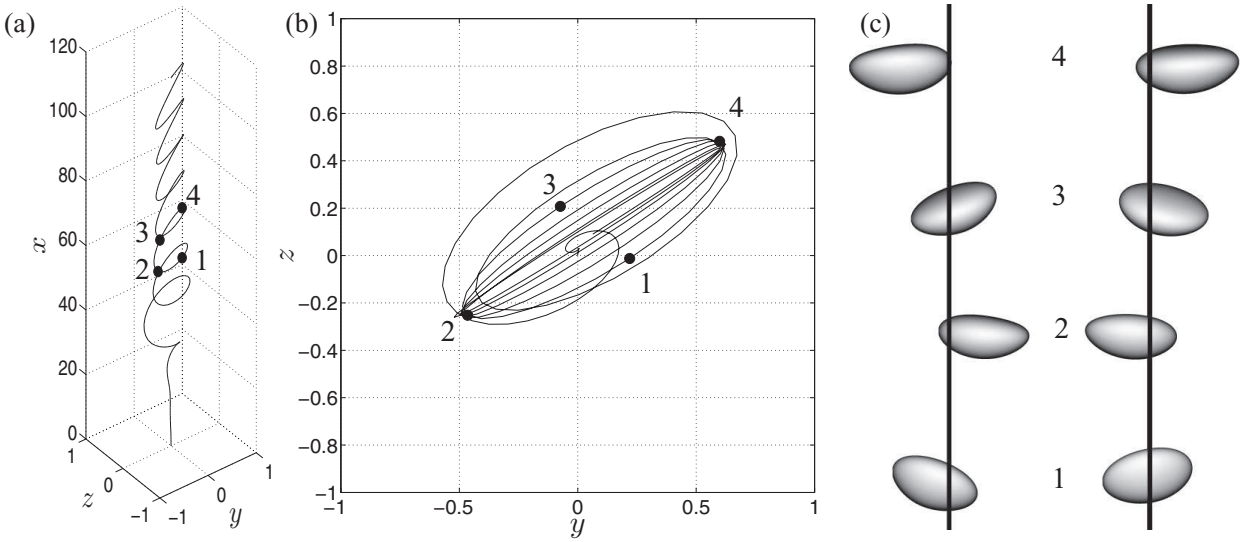

FIG. 13. Same as Fig. 12 for bubble number 16.

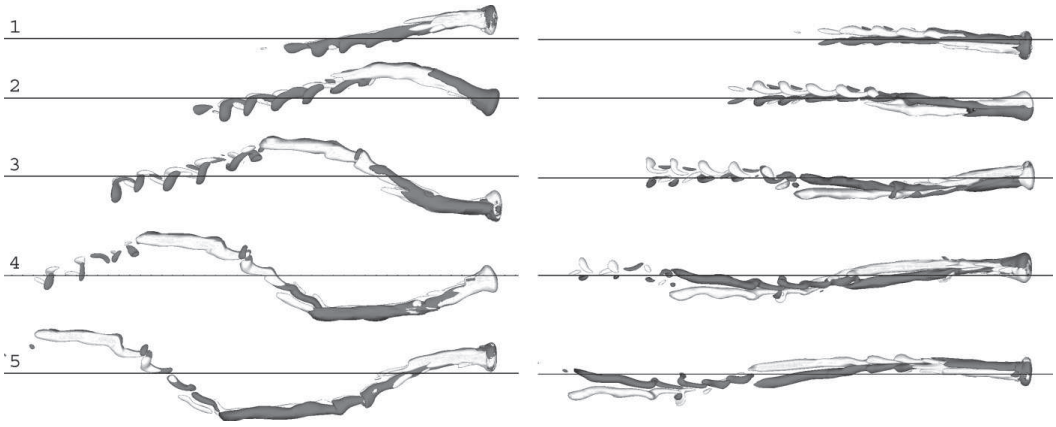

FIG. 14. Evolution of the streamwise vorticity isocontours $\omega_x = \pm 0.24$ at positions corresponding to the bullets shown in Figs. 12(a) and 12(b) for bubble number 5. The left and right panels display two perpendicular views and the solid line indicates the x axis.

different from the 4R mode previously identified in Fig. 9. Observations showing the existence of secondary vortex structures have repeatedly been reported in experiments performed in low-Mo fluids [4,26,51–53]. Here the wavelength associated with the secondary loops is somewhat larger than the spacing s_v between the two vortex threads, which might suggest that they result from Crow instability [54]. However, according to [4], the typical wavelength that emerges from Crow instability is in the range $5s_v$–$9s_v$, which is significantly larger than the characteristic wavelength revealed by Fig. 15. Hence it seems that this explanation has to be ruled out.

The most likely option left is that they result from the coupling between bubble deformation and wake dynamics, a coupling that has been studied in the past for larger bubbles having Reynolds numbers of $O(10^3)$ [51,55,56]. Indeed, every transient change in the bubble shape (especially in the vicinity of the bubble's equator) results in a change in the local curvature of the bubble surface, hence in a variation of the azimuthal surface vorticity. Once tilted in the streamwise (vertical) direction, the magnitude of the vorticity that enters the double-threaded wake reflects this change, yielding a modulation of the streamwise vortices. To assess this scenario, a simple test consists in comparing the typical wavelength of secondary loops, say, Λ, with the vertical distance traveled by the bubble during a period of the most likely shape oscillations, say, l_Ω, with $l_\Omega = 2\pi U_T/\Omega$, Ω being the radian frequency of the relevant oscillation mode. To estimate Ω, the most obvious choice is to consider that the dominant oscillations are those corresponding to mode 2. Ignoring effects of bubble oblateness on the frequency of this mode [35], we stay with the crude approximation $\Omega = \omega(2)$, which yields $l_\Omega/D = \frac{\pi}{2\sqrt{6}}\mathrm{We}_T^{1/2}$, where $\mathrm{We}_T = \rho U_T^2 D/\sigma$ is the Weber number based on the terminal rise velocity. Here $\mathrm{We}_T \approx 3.32$, so $l_\Omega/D \approx 1.17$. Independently, using Fig. 15, one deduces $\Lambda/D \approx 1.21$. Hence the two estimates are in excellent agreement, which gives strong support to the scenario of the secondary vortex loops resulting directly from the dominant shape oscillations through the variations of the vorticity they induce at the bubble surface. It must be pointed

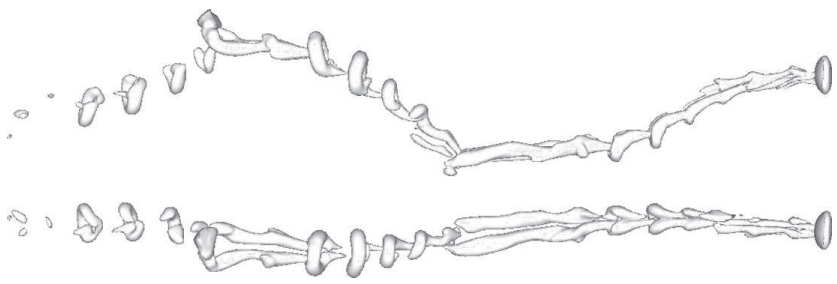

FIG. 15. Two perpendicular views of the wake structure past bubble number 5 revealed by the λ_2 criterion.

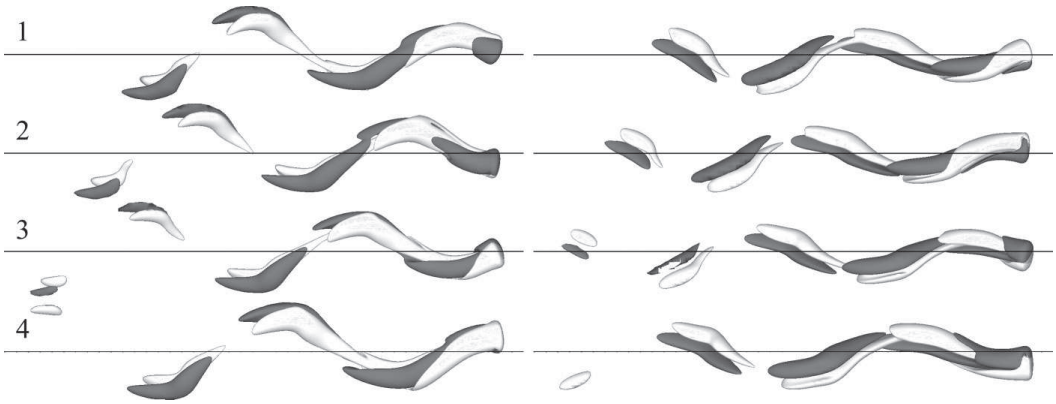

FIG. 16. Same as Fig. 14 for bubble number 16 (at a much earlier time than in Fig. 9).

out that this mechanism is not specific to the flattened spiraling regime: At a much later time, bubble 5 eventually follows a planar zigzagging path in which the wake structure remains similar, apart from the newly emerging planar symmetry, to that observed at earlier stages in Figs. 14 and 15.

Figures 16 and 17 show the wake structure past bubble number 16 using the same representations as in Figs. 14 and 15, respectively. These plots are taken at a much earlier time than in Fig. 9 to focus on the features specific to the flattened spiraling stage. The wake is of course characterized by a pair of intertwined streamwise vortices. However, the picture is now much simpler than with bubble number 5 since no short-wavelength loop exists. In this case, as already observed in Fig. 9, the wake structure is essentially of the 4R type, except that there is a significant twist of the connecting hairpins about the vertical axis. This wake structure results in a time-dependent lift force and torque with nonzero mean. Figure 18 shows a cross-sectional view of the vortical structure associated with this mode in different cross sections downstream of the bubble. The asymmetry between the negative and positive isocontours is clear, although not spectacular, and increases with the distance to the bubble. This distribution is reminiscent of that found in the yin-yang mode that emerges from the secondary Hopf bifurcation in the wake of a tethered infinitely thin disk [57] or from higher-order bifurcations in the case of thicker disks [58]. In both cases, the lift force oscillates about a mean direction. However, in the yin-yang mode the axial torque oscillates about a zero mean, whereas in the present case the mean axial torque is nonzero. This is why the bubble may keep a vertical path on average, whereas if the wake were in a true yin-yang mode, its average path would comprise a nonzero inclination. To conclude with this wake structure, it is worth examining briefly the reason why no secondary loops due to shape oscillations occur in this case. Using the same reasoning as for bubble number 5, one finds $l_\Omega/D \approx 1.27$, which is very close to the estimate obtained with the previous

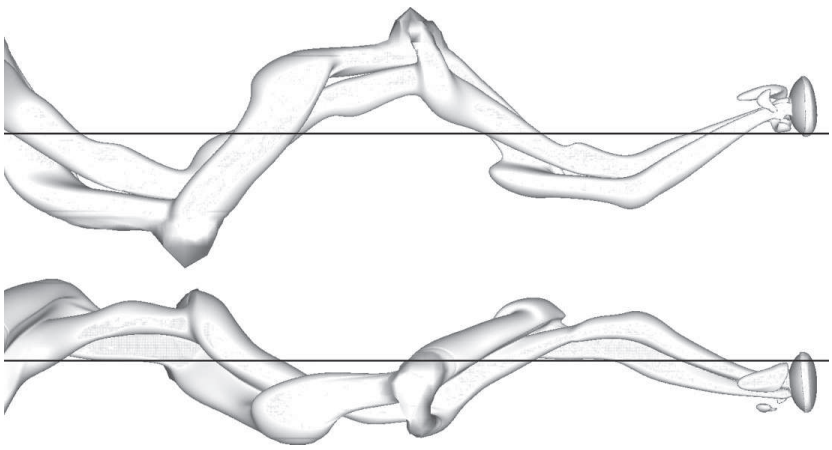

FIG. 17. Same as Fig. 15 for bubble number 16 (at a much earlier time than in Fig. 9).

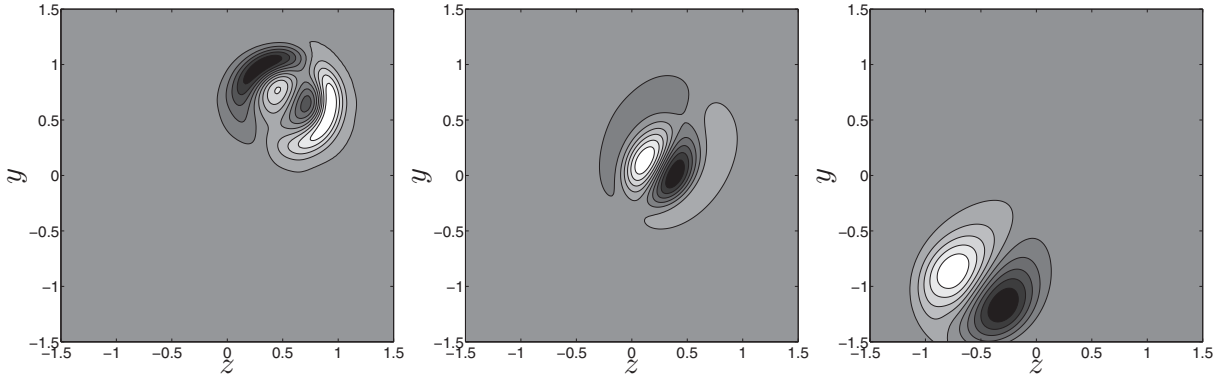

FIG. 18. Horizontal cuts showing the shape of the streamwise vorticity isocontours, from $\omega_x = -0.24$ (black) up to $\omega_x = 0.24$ (white) for bubble number 16 in cross sections located (from right to left) $0.5D$, $2D$, and $4D$ apart from the bubble centroid.

bubble. Hence the difference has to be found elsewhere. It lies in the ratio of the characteristic time of the oscillations $\omega(2)^{-1}$ over that of their viscous damping $\tau(2)$, i.e., in the oscillatory Reynolds number $\mathrm{Re}_{\mathrm{osc}} = \mathrm{Ga}\,\mathrm{Bo}^{-1/2}$. Compared with bubble number 5, the oscillatory Reynolds number is four times smaller in the present case, owing to the larger viscosity and smaller surface tension. Hence oscillations decay much faster and are unable to alter significantly the wake structure.

E. Chaotic regime

Chaotic motion of freely rising or falling bodies in which the path exhibits abrupt changes of direction and its horizontal projection tends to fill densely a part of the (y,z) plane has frequently been reported, especially with spheres and disks of various thicknesses [6]. Most of these observations are concerned with large-amplitude chaotic regimes that take place at *larger* values of the control parameter than well-defined regimes such as planar zigzag (see, e.g., [59–61]). For instance, it has been observed with light rising spheres [59] that increasing the Galilei number (the body-to-fluid density ratio being kept fixed) yields successively rectilinear, steady oblique, oscillating oblique, planar zigzagging, and chaotic paths. Similar observations have been reported with rising bubbles, i.e., in a given fluid, chaotic (frequently referred to as rocking) motions are observed for bubble diameters larger than those giving rise to zigzagging and spiraling paths [2,51,62].

Here we are concerned with another type of chaotic path that, for a given value of Mo, was detected in several simulations carried out with slightly *smaller* values of the Galilei number than those at which zigzagging paths (and during long transients, flattened spiraling paths) were encountered. This chaotic regime was observed for bubbles 2, 3, 7, 8, and 9 in Fig. 4, which all belong to the two low-Mo series. These bubbles follow nearly vertical trajectories on which small-amplitude horizontal displacements, exhibiting abrupt changes of direction, superimpose, as shown for bubble 3 in Figs. 19(a) and 19(b); this bubble motion is accompanied by a thin double-threaded wake that grows and sheds streamwise vorticity in an aperiodic manner [Fig. 19(c)]. Path instability was already detected experimentally in Ref. [4] for the (Bo,Ga) pair corresponding exactly to bubble 3, a result that was later on corroborated numerically in Ref. [23]. That these computations, where the bubble shape was kept frozen, captured the corresponding path instability proves that shape oscillations are not at the root of the latter in this region of the (Bo,Ga) plane.

According to Fig. 19(b), the amplitude of the horizontal bubble displacements is approximately $0.15D$ from crest to crest, in contrast to the $2.3D$ amplitude revealed by Fig. 12 for the slightly larger bubble number 5, which follows a flattened spiraling and then a planar zigzagging trajectory. The bubble shape also experiences small fluctuations, mainly in the back region, the corresponding changes of the aspect ratio (with is about 1.75 on average) being less than 5%. It is interesting to notice

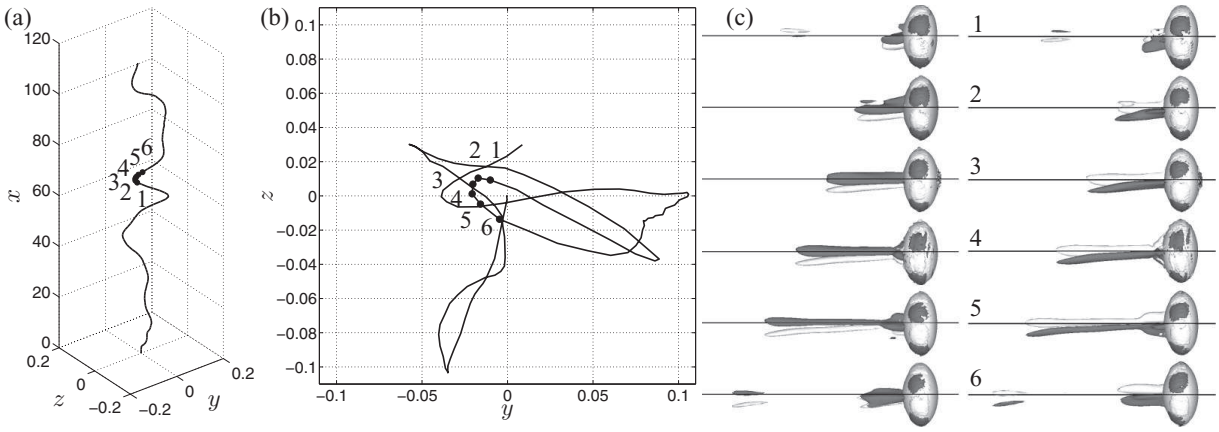

FIG. 19. (a) Three-dimensional reconstruction and (b) top view of a bubble trajectory typical from the chaotic regime (bubble number 3). (c) Evolution of the streamwise vorticity isocontours $\omega_x = \pm 0.24$ corresponding to the bullets shown in (a) and (b); time and x coordinate increase from top to bottom; on the left is the x-z plane and on the right, the x-y plane. The solid lines in (c) indicate the x axis.

that all six snapshots in Fig. 19(c) reveal the existence of a symmetry plane in the wake; however the orientation of this plane changes over time since it always has to remain locally tangent to the path.

A key feature of the base flow associated with the present chaotic regime may be inferred from Fig. 4 by examining the dashed line corresponding to the critical curve beyond which a standing eddy takes place. Clearly bubbles 2, 3, 7, and 8 stand below this curve, hence there are no closed streamlines in the corresponding base flows. The reason why this feature is important here is that the existence of a standing eddy is known to be a necessary condition for the onset of wake instability past fixed bluff bodies. Indeed, this instability is absolute in nature and finds its root in the wavemaker located in the core of the standing eddy [63]. Hence the path instability observed in the present regime does not result from a wake instability and must be seen as an outcome of the coupling between the bubble and the surrounding flow. Similar examples are known to exist with disks of various thicknesses [64,65], although they are less spectacular because a small standing eddy is still present. The reason why the coupled fluid-body system may become unstable at Reynolds numbers much smaller than the threshold value for the same body held fixed was identified in Ref. [65], where a LSA of the whole system was carried out. It was shown that, in addition to the eigenmodes associated with wake instability, the coupled system exhibits other eigenmodes that result from the constraint that the overall force and torque balances on the body put on its angular orientation and rotation rate (see also [66]). Under certain conditions, these modes can become unstable at lower Reynolds number than the former ones, so the path instability may occur even though the wake is still stable. This is what happens here and the double-threaded wake displayed in Fig. 19(c) is just enslaved to the path, i.e., it is a consequence of the lateral excursions of the bubble, not their cause.

Given the small amplitude of the horizontal bubble displacements in Fig. 19, as compared with those found in the well-defined zigzagging and spiraling regimes, it is clear that the present chaotic paths are associated with the generic family of the so-called A regimes described in Ref. [6]. These quasivertical, albeit unstable, regimes are frequently encountered with thin disks. They generally precede a transition to a large-amplitude zigzagging regime, which is often subcritical. This is the case, for instance, with slightly buoyant disks with an aspect ratio $\chi = O(10)$ for which a series of five quasivertical regimes, the first of which is steady oblique whereas the last one is chaotic, is succeeded by a subcritical transition to a well-defined planar zigzagging state [64,67]. Here the chaotic regimes identified with bubbles 2 and 3 in pure water are succeeded by a transitional regime for bubble 4 in which the bubble "hesitates" between a chaotic and a flattened spiraling path, both of which display $O(D)$ horizontal displacements. Then bubble number 5, the largest in this series, eventually zigzags in a plane after having followed a flattened spiraling path during a very long time. Similarly, with the slightly larger Morton number $\mathrm{Mo} = 1.8 \times 10^{-10}$, the chaotic regime identified

with bubbles 7 to 9 is succeeded by a large-amplitude planar zigzagging regime for bubbles 10 and 11. Hence the present findings for the lowest two Mo are consistent with a scenario in which the system first undergoes a primary bifurcation where the vertical axisymmetric regime is succeeded by a chaotic (hence three-dimensional) *A* regime and then a secondary bifurcation from which a planar zigzagging regime emerges after a more or less long transient stage during which the bubble follows a flattened spiraling path.

The reason why LSA is unable to predict the instability of the fluid-bubble system throughout the parameter range where DNS detects this small-amplitude chaotic regime needs clarification. The difference between the two series of predictions is not thin, since LSA predicts that only bubbles with $\chi \gtrsim 2.20$ (or $\chi \gtrsim 2.15$ when a strictly spheroidal shape is assumed) can exhibit a nonvertical path, whereas bubble 2, which has the smallest oblateness of all unstable bubbles considered in this study, corresponds to $\chi \approx 1.65$. As discussed in Ref. [24], a plausible explanation could be that the instability sets in before the base flow has reached the strict steady state assumed in the LSA approach, given the high Reynolds number ($\mathrm{Re} \gtrsim 600$) at which the phenomenon takes place in the low-Mo range. This remains a possibility and could perhaps be checked by introducing a slowly time-dependent base flow in the LSA approach. However, the resemblance between the chaotic *A* regime revealed by DNS and the recent discovery of similar regimes preceding a sub- or supercritical transition to a zigzagging regime for thin disks [64,67] suggests another potential scenario that was very unlikely before the present results were obtained: The transition from a steady vertical path to quasivertical chaotic paths could be subcritical, in which case it would not be captured by LSA. If so, starting from the vertical axisymmetric regime and increasing gradually the bubble diameter, i.e., Bo and Ga, in the presence of infinitesimal disturbances, the system would switch directly at some point to a finite-amplitude zigzagging regime, a transition that would correspond to the threshold predicted by LSA. From that point, decreasing gradually the bubble diameter, the system would enter the quasivertical chaotic regime until jumping back to the steady vertical regime. Such a scenario would imply that the entire parameter range where the chaotic regime is observed would actually correspond to a region of bistability. Exploring this possibility demands very large CPU resources, owing to the numerous runs required to achieve a step-by-step increase and decrease of Bo and Ga, and is beyond the scope of this study. Nevertheless, data from [4] give some support to this hypothesis because straight vertical paths and zigzagging or spiraling paths were both observed in the range $0.31 \leqslant \mathrm{Bo} \leqslant 0.36$ in these experiments.

IV. EVOLUTION OF THE RISE VELOCITY AND UNDERLYING MECHANISMS

Figure 20 shows the evolution of the Reynolds number $\mathrm{Re} = \rho D U/\mu$ for the various flow regimes discussed in Sec. III and defined in Table I. Tiny oscillations due to the numerical procedure employed to determine the rise velocity may be noticed in some cases, e.g., in Fig. 20(a); nevertheless, they remain much smaller than those shown in Figs. 20(b)–20(e), which are associated with path instability. In all cases, the rise velocity increases linearly during a first period of time. Within this initial stage, the dominant force acting on the bubble (apart from buoyancy) is the so-called added-mass force, which is proportional and opposed to its acceleration dU/dt^*. The viscous drag force does not play a significant role yet, being proportional to $U(t^*)$, since the flow is nearly irrotational. As far as the bubble remains spherical, the amount of fluid it displaces is half its own volume, yielding an added-mass coefficient $C_M = 1/2$. Hence the rise velocity initially evolves as $U(t^*) \approx 2gt^*$. At the same time, the Weber number $\mathrm{We}(t^*) = \rho U^2(t^*) D/\sigma$ increases quadratically over time and becomes of $O(1)$ when $t^* = t_1^* = (\sigma/4\rho g^2 D)^{1/2}$, i.e., $t_1 = (4\,\mathrm{Bo})^{-1/2}$. At that time, the bubble has already become somewhat oblate, owing to the pressure difference that has established between its poles and equator. This tendency goes on for $t > t_1$. One consequence of this deformation is that the bubble displaces more fluid as it rises, so its added-mass coefficient $C_M(t^*)$ increases significantly over time (according to [33] $C_M \approx 1.12$ for $\chi = 2$). Moreover, the Reynolds number is already large when $t = t_1$, since $\mathrm{Re}(t_1) = (\rho\sigma D/\mu^2)^{1/2} = \mathrm{Ga}\,\mathrm{Bo}^{-1/2}$, and goes on increasing at later times. The combined effect of this increase in C_M with that of the

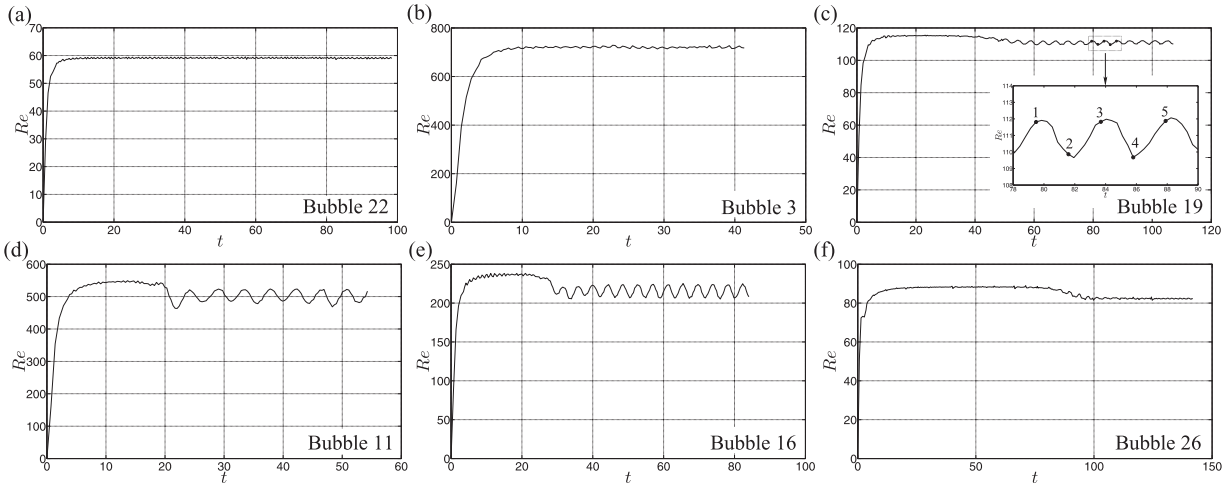

FIG. 20. Evolution of the Reynolds number for different bubbles in Table I: (a) rectilinear regime, (b) chaotic regime, (c) planar zigzagging regime, (d) and (e) flattened spiraling and then planar zigzagging regime, and (f) spiraling (helical) regime. In (c) the inset shows a detailed view of the oscillations and the numbers identify the instants of time 1–5 of Figs. 6 and 7.

viscous drag force, which is still almost proportional to $U(t^*)$ but now involves a prefactor $G(\chi)$, which is also an increasing function of χ [with $G(1) = 1$], is a progressive decrease of the bubble acceleration. Hence the rise velocity does not increase linearly anymore when $t \gtrsim t_1$, since the buoyancy, added-mass, and viscous drag forces have a similar order of magnitude and the latter two involve coefficients that depend on χ, which itself varies in a nonlinear manner with the current Weber number $\mathrm{We}(t^*)$ (see [68]). At some point, the added-mass force becomes negligible and the bubble reaches a quasiterminal rise velocity U_{QT}, resulting from a balance between the buoyancy force and the viscous drag force $-6\pi\mu D G(\chi) U_{QT}$. This yields the estimate $U_{QT} \approx \rho g D^2/36\mu G(\chi)$, i.e., a nearly terminal Reynolds number $\mathrm{Re}_{QT} \approx \mathrm{Ga}^2/36G(\chi)$. For instance, in the case of bubble number 3, which corresponds to $\mathrm{Ga} = 255.3$, the final oblateness is about 1.75, so $G(\chi) \approx 2.25$ and $\mathrm{Re}_{QT} \approx 805$ [68], which provides the right order of magnitude of the terminal Reynolds number since Fig. 20(b) indicates $\mathrm{Re}_T \approx 720$. The time at which this happens, say, $t^* = t_2^*$, may be estimated by assuming that the rise velocity evolves approximately as $U(t^*) = U_{QT}(1 - e^{-t^*/\beta})$ up to $t^* = t_2^*$. Keeping in mind that $dU/dt^* \approx 2g$ at short times, i.e., $\beta = \rho D^2/72\mu G(\chi)$, and considering that the exponential contribution becomes negligible when $t^* \approx 4\beta$ (since $e^{-4} < 0.02$), i.e., $t_2^* = 2U_{QT}/g$, one obtains in dimensionless form $t = t_2 = \mathrm{Ga}/18G(\chi)$, i.e., $t_2 \approx 6.3$, which again agrees quite well with the time at which the early evolution of the Reynolds number ends according to Fig. 20(b).

Throughout this early evolution, vorticity is continuously generated at the bubble surface, yielding the formation of a boundary layer around it and an axisymmetric wake downstream. However, owing to the specificities of the shear-free condition as compared with the usual no-slip one (see below), vorticity remains finite within the boundary layer as the Reynolds number becomes large. This in turn implies that the vortical regions only result in a final $O(\mathrm{Re}_T^{-1/2})$ relative correction to the viscous drag force [68] that does not alter the above estimates at leading order. As mentioned in Sec. III, a key feature of vorticity dynamics around uncontaminated bubbles is that surface vorticity is proportional to the product of the relative fluid velocity by the local interface curvature [40]. For this reason, it may be shown [18] that the azimuthal vorticity ω_θ and the vorticity flux $\mu\partial\omega_\theta/\partial n$ at the surface of an oblate bubble ($\partial/\partial n$ standing for the derivative in the direction normal to the surface) vary as $\chi^{8/3}U_T/D$ and $\mathrm{Re}_T^{-1/2}\chi^{7/2}\rho U_T^2/D$, respectively [strictly speaking, these estimates are valid only in the limit of large χ, but they actually apply even down to $\chi = O(2)$]. The $\mathrm{Re}_T^{-1/2}\chi^{7/2}$ prefactor in the latter estimate implies that the viscous vorticity flux that enters the flow may be of the same order as the advective flux $\rho U_T \omega_\theta$, even at large Reynolds number, provided the bubble oblateness is sufficient. This is why, beyond some critical oblateness that depends on the Reynolds number,

vorticity accumulates within a standing eddy at the back of the bubble. Having reminded these fundamental properties, one can also determine the various time scales involved in the development of vortical regions, keeping in mind that the distance δ_T over which vorticity diffuses within a time interval T^* is $\delta_T \approx (2\mu T^*/\rho)^{1/2}$. First, the time required for the boundary layer to reach its final thickness $\delta_V \approx (D/2)\mathrm{Re}_T^{-1/2}$ is obtained by equating δ_T and δ_V, which yields $T_V^* \approx D/8U_T$. Vorticity is also advected downstream in the wake with an $O(U_T)$ velocity, so the corresponding time scale, say, T_W^*, is again of $O(D/U_T)$. Hence, in both cases, the dimensionless characteristic time is proportional to Ga^{-1}. Things are different regarding the growth of the standing eddy whose size does not scale with δ_V. As shown in Fig. 5, it rather scales with D, provided the distance to the threshold $\mathrm{Ga} = \mathrm{Ga}_s(\mathrm{Bo})$ beyond which a standing eddy exists at the current value of Bo (dotted line in Fig. 4) is large enough. Thus the corresponding time scale, say, T_S^*, is $T_S^* = \rho D^2/2\mu$, i.e., $T_S = \mathrm{Ga}/2$. Hence, under such circumstances, the longest time scale involved in the development of vortical regions is the one associated with the growth of the standing eddy and this is why, when Ga is large, the base flow may not be completely stationary at the time the instability sets in.

After the bubble has reached its quasiterminal velocity, path instability may in principle take place provided Ga exceeds the threshold value $\mathrm{Ga}_c(\mathrm{Bo})$ corresponding to the solid line in Fig. 4. It does so almost immediately in the chaotic regime, as may be observed in Fig. 20(b), which corresponds to a situation in which no standing eddy exists. In contrast, in most other cases, there is a significant delay between the time at which U_{QT} is reached and that at which some further evolution of $U(t^*)$, such as oscillations, happens. Considering the position of bubbles corresponding to Figs. 20(c)–20(f) in the (Bo,Ga) diagram of Fig. 4 reveals that they all stand above the dashed line, i.e., they all correspond to $\mathrm{Ga} > \mathrm{Ga}_s(\mathrm{Bo})$. This is in line with our estimates of the time scales associated with the vortical regions and the observed delay may be interpreted as the time period T_S required for the development of the standing eddy. Obviously T_S depends on $\mathrm{Ga} - \mathrm{Ga}_s(\mathrm{Bo})$, hence on Ga and Bo. This is reflected in Fig. 20, where the duration of the corresponding plateau is seen to increase significantly with Bo [bubble 11 in Fig. 20(d) has $\mathrm{Bo} = 1.0$, while bubble 26 in Fig. 20(f) has $\mathrm{Bo} = 10.0$].

Once this development is completed, path instability sets in provided $\mathrm{Ga} > \mathrm{Ga}_c(\mathrm{Bo})$, yielding a significant decrease of the rise velocity whatever the next style of path. The reason for this decrease is twofold. First, as soon as the bubble starts oscillating, part of the potential energy of the system is spent in the generation of its horizontal motion rather than its rise. Second, compared with the axisymmetric flow structure, wakes associated with nonstraight paths are three dimensional and involve larger velocity gradients, resulting in a larger viscous dissipation, hence a larger drag. Not surprisingly, when the subsequent regime corresponds to a helical path [Fig. 20(f)], the rise velocity reaches a constant final value, in line with the constant force and torque delivered by the spiral wake displayed in Fig. 11. In cases in which the bubble rather follows a zigzagging or a flattened spiraling path, the decrease of U is succeeded by oscillations whose amplitude depends of course on that of the lateral bubble displacements. Similar oscillations have been reported in experiments [69,70] and DNS [21] at higher Reynolds numbers. The corresponding frequency is twice that of the lateral motion since the drag force is an even function of the bubble inclination with respect to the vertical. These oscillations result from the two mechanisms mentioned above, as can be understood more easily in the case of a planar zigzag. First, the buoyancy force has an oscillating horizontal component that reaches its maximum at the inflection point of the zigzag and vanishes at each of its extremity. Hence, if the wake were axisymmetric, the rise velocity would go through a minimum (maximum) at the former (latter) position. Second, since the actual wake structure is dominated by a pair of counterrotating trailing vortices, the vortex cores, which are low-pressure regions, increase the pressure difference between the front and back regions of the bubble, yielding an additional drag that may be thought of as a "sucking" of the bubble by its wake. This is nothing but the classical induced drag acting on a wing of finite span. However, here the streamwise vorticity changes its sign twice during a zigzag period. As we saw in Sec. III, this change takes place approximately midway between the extremity of the zigzag and the inflection point, i.e., in between points 1 and 2 (3 and 4) during the first (second) half-cycle of the zigzagging path displayed in Fig. 6. Consequently, the lift and induced-drag forces vanish at these positions. Combining the two mechanisms, one expects the

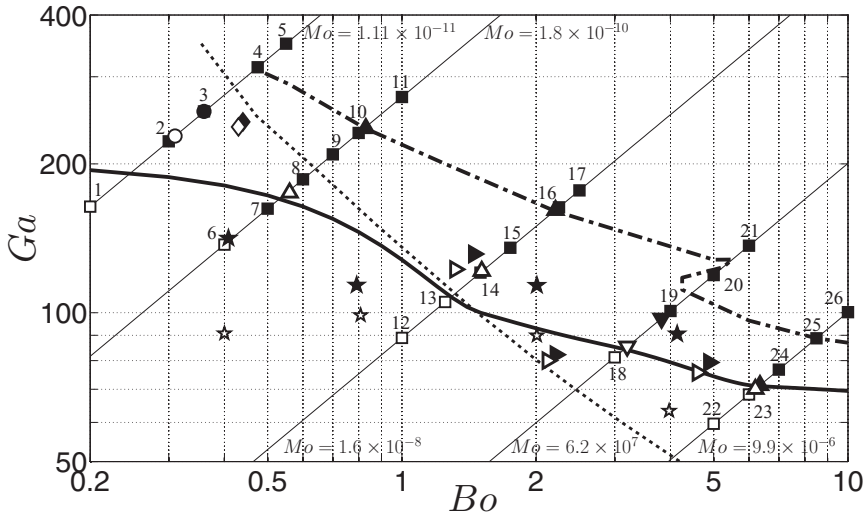

FIG. 21. Comparison between present predictions (open and closed squares, same definition as in Fig. 4) and critical conditions determined in various works. Data are shown for the DNS of Ref. [29] (⋆); the experiments with ultrapure water of Refs. [14] (⧫) and [4] (●); and the experiments in various silicon oils of Refs. [9] (▲), [10] (▼), and [11] (▶). In these data sets, the open (closed) symbols correspond to the largest stable (smallest unstable) bubble. The three curves are identical to those in Fig. 4.

rise velocity to reach its maximum slightly after each extremity of the zigzag, i.e., just after positions 1 and 3 in Fig. 6, which is fully confirmed by the evolution displayed in the inset of Fig. 20(c).

V. REGIME MAP AND CRITICAL CONDITIONS FOR PATH INSTABILITY

A. Observed transitions

We now return to the critical conditions that define the onset of path instability and to the succession of unstable regimes revealed by this study. Results corresponding to the 26 bubbles we considered are gathered in Fig. 21, together with the critical curves previously obtained by assuming frozen bubble shapes and several experimental and computational results from the literature that we consider state of the art. In particular, all experimental data reported in that figure correspond to surfactant-free conditions because they were obtained either in ultrapure water [4,14] or in silicon oils [9–11], which are nonpolar liquids. In the following discussion it must be kept in mind that, of the two critical curves reported in Fig. 21, that provided by the LSA approach may be considered as "exact" in the sense that it resulted from a detailed exploration of the (Ga,Bo) space based on small steps in both parameters, whereas that provided by the frozen-shape DNS is much more qualitative since it was deduced from a series of runs in which these steps were much larger. The figure also indicates the nature of the final path we observe, but it must be pointed out that this may not be the ultimate regime: In Ref. [21] the path of a bubble corresponding approximately to $\mathrm{Bo} = 0.85$ and $\mathrm{Ga} = 390$ was found to undergo a transition from planar zigzag to spiral after the bubble rose approximately $250D$ above its initial position. Here the numerical domain is only $128D$ high, so it may well be that in certain cases the regime indicated in the figure would be succeeded by a different one if we could follow the bubble over a longer time.

For $\mathrm{Bo} > 5$, the critical conditions drawn by the present study agree well with those found in Ref. [23], which employed a different code. Since the shape was frozen in that case, this agreement suggests that shape oscillations do not modify significantly the threshold of path instability in that high-Bo range, although surface tension effects are weak. In the intermediate range $1 \leqslant \mathrm{Bo} \leqslant 5$, the present results yield a threshold somewhat larger than indicated by the results of [23], i.e., the path of three-dimensional deformable bubbles looks slightly more stable than that of frozen axisymmetric bubbles. Things are different in the low-Bo range (i.e., $\mathrm{Bo} < 1$) where the low-amplitude chaotic

regime was detected for some (Bo,Ga) pairs located significantly below the critical curve of [23] (e.g., bubble 7), suggesting that the instability may be triggered by shape oscillations in that range.

Apart from this chaotic regime, the other unstable regimes revealed by the DNS are essentially those documented in the literature. For a given Mo, the generic succession encountered when the bubble diameter is increased starts with a planar zigzagging regime, which may or may not emerge from a (frequently long) transient during which the bubble follows a flattened spiraling path. These two possibilities indicate that the first bifurcation does not necessarily preserve a symmetry plane, the latter emerging at a later time if the flattened spiraling regime first takes place. It must be kept in mind that an arbitrary linear combination of two counterrotating helices with the same frequency and opposite orientations results in a flattened spiral; it degenerates into a planar zigzag in the particular case where the two amplitudes are equal and in a circular helix if one of them is zero. Hence all three types of path are equivalent from the point of view of linear stability. The fact that the first nonvertical path that emerges in the present DNS is frequently a flattened spiral suggests that the discrete description of the axisymmetric bubble surface on the three-dimensional Cartesian grid induces some differences in the amplitudes of the two counterrotating linearly unstable helical modes.

Increasing the bubble diameter again, the planar zigzagging regime is succeeded at some point by a spiraling one in the series corresponding to the highest Morton number considered here (bubble 26). This change of style is associated with the loss of the planar symmetry in the wake, as shown in Fig. 11. With bubbles rising in pure water, the transition from planar zigzag to spiral, for instance, was observed to take place in the range $2.2 \leqslant \chi \leqslant 2.3$ (i.e., $1.6 \leqslant \mathrm{Bo} \leqslant 1.75$) in Ref. [51]. Hence it probably exists for all values of the Morton number considered here, but we did not explore a sufficiently large range of Ga for most of them to confirm this.

Examination of Table I reveals two clear trends regarding the variations of the Strouhal number. First, for each value of Mo, the larger the bubble (i.e., Bo and Ga), the larger St, irrespective of the detailed geometry of the corresponding nonvertical regime. This tendency, which is in line with past observations at higher Reynolds number [56], results from the increasing oblateness of the bubble as D increases, which in turn increases the amount of vorticity generated at its surface. Second, the Strouhal number is seen to increase uniformly with Mo: Focusing on the zigzagging regime, St is about 0.045 when $\mathrm{Mo} = 1.1 \times 10^{-11}$ and increases up to 0.136 when $\mathrm{Mo} = 9.9 \times 10^{-6}$. This is because the larger the Morton number, the smaller the critical Reynolds number corresponding to Ga_c and the larger the bubble oblateness, hence the more intense the vorticity flux generated at the bubble surface, owing to the $\chi^{7/2}\mathrm{Re}^{-1/2}$ scaling obeyed by this flux. This variation of St with Mo agrees qualitatively with LSA predictions: For $\mathrm{Bo} \leqslant 1.2$ (which holds throughout the series corresponding to the lowest two Mo), the latter indicate that the first unstable mode is of low-frequency type with a Strouhal number about 0.02, whereas for $\mathrm{Bo} \geqslant 5.5$ (which holds throughout the series corresponding to the largest Mo) it is of high-frequency type with $\mathrm{St} = O(0.1)$. In contrast, in the intermediate range $1.2 < \mathrm{Bo} < 5.5$, LSA predicts that the first unstable mode is stationary, which corresponds to a steady oblique path. Although such a path has often been reported for freely rising and falling rigid spheres [38,59] and disks [64,67,71] and results from a subtle nontrivial zero-torque condition that was derived through a weakly nonlinear analysis for both geometries in Ref. [72], it has never been observed in experiments or in DNS with bubbles. The present results for the two intermediate series $\mathrm{Mo} = 1.6 \times 10^{-8}$ and 6.2×10^{-7} do not escape this rule, as they show that the first nonvertical regime encountered within that range is always of the planar zigzagging type. The reason might be that the zero-torque condition cannot be satisfied by a shear-free bubble rising along a steady inclined path, a hypothesis that could be checked by extending the theory developed in Ref. [72] to bubbles.

B. Toward a well-defined critical curve: Current consensus and open questions

Figure 21 also contains several pairs of experimental and numerical data that, for a given fluid, correspond to the largest (smallest) bubble that was found to follow a straight (nonstraight) path, i.e., the largest and smallest bubbles such that $\mathrm{Ga} < \mathrm{Ga}_c(\mathrm{Bo})$ and $\mathrm{Ga} > \mathrm{Ga}_c(\mathrm{Bo})$, respectively. Let us first

examine how the present findings compare with critical conditions determined from experiments, keeping in mind that the (Bo,Ga) step separating the last stable point from the first unstable one in the available data sets is often quite large. The agreement is clearly satisfactory for the highest three Mo, i.e., there is a consensus between the present DNS results and experiments that path instability sets in approximately at $\mathrm{Ga}_c \approx 70$, 90, and 125 for $\mathrm{Mo} = 9.9 \times 10^{-6}$, 6.2×10^{-7}, and 1.6×10^{-8}, respectively. The situation is less clear for the lowest two values of Mo. According to [9], the paths observed in silicon oil corresponding to $\mathrm{Mo} = 1.8 \times 10^{-10}$ remain rectilinear up to $\mathrm{Bo} = 0.56$, whereas we already observed a low-amplitude chaotic regime for bubble number 7, i.e., with $\mathrm{Bo} = 0.50$. Similarly, in pure water, all paths were found to be rectilinear up to $\mathrm{Bo} = 0.31$ in Ref. [4], whereas we already observed a chaotic path for bubble number 2, which corresponds to $\mathrm{Bo} = 0.30$. However, the amplitude of the bubble lateral shift in the chaotic regime is so small [typically of $O(0.1D)$] that it may not have been detected in experiments, despite the modern optical tools that were employed. A similar situation is known to exist with thin cylinders whose tiny lateral displacements were not resolved in experiments [73] but were clearly identified in DNS [64,67].

Four other pairs of data reported in Fig. 21 were extracted from a recent computational study [29], also performed with the GERRIS code. Although the critical conditions that can be inferred from these data are in good qualitative agreement with the present ones for $\mathrm{Bo} \geqslant 2$, they result in significantly lower values of Ga_c for $\mathrm{Bo} \leqslant 1$. Such low values are clearly not supported by experiments, suggesting that the grid employed in Ref. [29] is not sufficient to capture accurately the small-scale vortical regions involved in the initiation of the instability in the low-Mo (hence high-Ga) range. Indeed, this grid had a resolution about half the present one. Hence, although it is probably suitable for dealing with the high-Bo part of the transitional region where $\mathrm{Re}_T = O(10^2)$, it is certainly not sufficient to address properly the low-Bo part where Re_T may be up to 900, which implies a reduction of the boundary layer thickness by a factor of 3. This remark also questions the adequacy of the grid used in the present investigation in that regime, where typically three grid cells stand within the boundary layer, which is barely sufficient. The grid density in the near wake is one-fourth the latter, so the smallest vortical structures are also probably overlooked. Therefore, although we are confident that the corresponding results are almost quantitatively correct, it would be desirable to double the grid density, at least in the vortical regions, to achieve grid convergence.

Finally, although this is not the subject of the present paper, the significant quantitative differences, about 25% for $\mathrm{Bo} \geqslant 5$, between the approximate threshold resulting from the DNS of [23] and that provided by the LSA approach of [24], both based on the frozen-shape hypothesis, remain to be explained. They may result, at least in some parts of the Morton number range, from numerical inaccuracies in either code, from the hypothesis of a strictly stationary base flow in the latter [but this was found to have no effect in the case of disks with $O(10^2)$ Reynolds numbers for which the comparison of the two approaches revealed excellent agreement [65]], or from the subcritical nature of the primary bifurcation, although no indication of such a behavior was noticed up to now, except perhaps in the low-Mo range. This has to be clarified in the future.

VI. CONCLUSION

In this work we examined the results of a series of 26 three-dimensional numerical simulations of the flow past freely deforming bubbles rising in still liquids. We selected the physical parameters so as to cover approximately the transition region where path instability is expected to take place over four orders of magnitude of the Morton number. We varied the Bond number by two orders of magnitude (from 0.1 to 10) and the Galilei number by a factor of 6, from $\mathrm{Ga} \approx 60$ in the most viscous case to $\mathrm{Ga} \approx 350$ in the most inertial one, which corresponds to a variation of the terminal Reynolds number by a factor of 15 (from $\mathrm{Re}_T \approx 60$ to $\mathrm{Re}_T \approx 880$). Depending on the value of the dimensionless parameters, we observed contrasting evolutions, starting in each series with a rectilinear rise associated with an axisymmetric wake. Beyond the transition, four types of path were identified. Three of them have been widely described in the literature, namely, planar zigzag and circular spiral (or helix), plus the intermediate flattened spiraling path. The last one is a low-amplitude

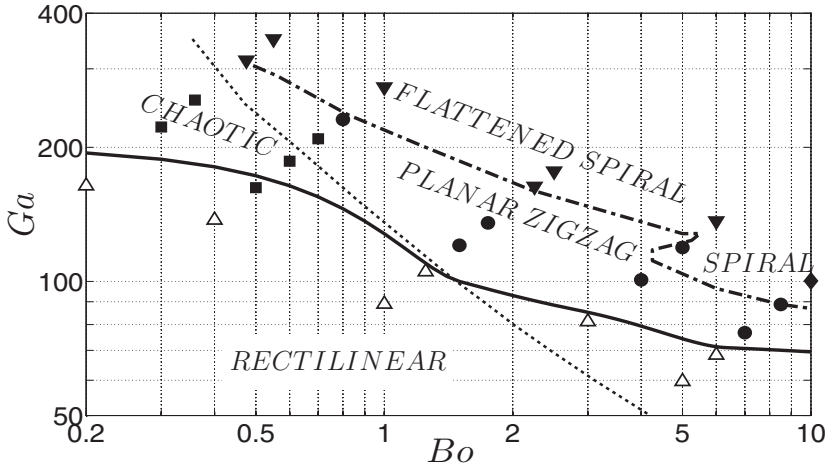

FIG. 22. Phase diagram summarizing the different styles of path observed in present simulations (rectilinear, △; planar zigzag, •; flattened spiral, ▼; spiral (helical), ♦; and chaotic, ■). The three curves are identical to those in Fig. 4.

chaotic path. The location of the 26 runs in the (Bo,Ga) plane and the style of the corresponding final paths observed in the various regions or this plane are summarized in Fig. 22.

The zigzagging regime is characterized by a periodic lateral motion of the bubble on both sides of an average vertical path. The amplitude, which is of the order of the bubble diameter, and frequency of these horizontal movements have been found to be increasing functions of the Bond number. An important result of this investigation is the significant nonaxisymmetric deformation that takes place, for large enough Bond numbers, every time the bubble goes through an extremity of the zigzag. Indeed, it was found that, for Bo $= O(5)$, its rotation induces pressure differences along the equator that can exceed 10% those between the upper pole and the equator. This yields bubbles with a significantly larger curvature on the side looking toward the exterior of the zigzag. In this regime, the wake is dominated by a double-threaded structure exhibiting a planar symmetry. However, two different vortex shedding modes were identified. The most common is the 2R mode, which corresponds to a wake made of a two-sided chain of vortex loops in which vorticity changes its sign every half-cycle in between the extremity of the zigzag and its centerline. In contrast, in other cases, the wake structure is dominated by a 4R mode in which a second single-sided loop superimposes onto the primary one, being generated in between two successive changes of sign of the primary vortex threads. In line with the original observations of this regime with falling spheres [38], we found that the style of the shedding mode is closely linked to the amplitude of the oscillations in the rise velocity: When these oscillations are small [typically of $O(10^{-2}U_T)$], the wake is of the 2R type, whereas the 4R structure emerges when they become one order of magnitude larger.

The circular spiraling or helical regime was only observed in one of the runs performed at the highest Morton number, most probably because we did not consider large enough values of the Galilei number in the other series. In this regime, no symmetry plane exists in the wake that consists of two disconnected and intertwined threads of streamwise vorticity, resulting in a corkscrew structure. This wake structure remains frozen as the bubble rises and results in a constant rise velocity, in line with previous findings with spheroidal bubbles [21,25]. Although it has been reported in some experiments that the path may switch directly from rectilinear to spiral, the present observations suggest that spiraling paths can only arise after planar zigzags, i.e., either for larger bubble diameters or after a long planar zigzagging transient.

The above two "pure" nonvertical paths frequently emerge after a more or less long transient during which the bubble follows a flattened spiraling path, which may be thought of as a slowly precessing planar zigzag whose precession rate varies over time. This regime is frequently observed over rising distances of $O(10^2 D)$, so in some cases we could not determine whether or not it

would have converged toward one of the two pure limits had the numerical domain be much higher. As far as the period of the zigzagging component is much shorter than that of the precession, most characteristics of this regime display trends similar to those observed in the planar zigzagging regime. The most specific features reside in the wake where the two vorticity threads are more or less severely twisted, yielding a nonzero time-averaged lift force and axial (i.e., vertical) torque. The corresponding shedding mode may be of the 2R or 4R type, similar to the planar zigzagging regime. Under certain conditions, a spectacular change in the wake structure was observed (it also happens in the planar zigzagging regime), namely, the occurrence of series of secondary vortex loops whose frequency was shown to be very close to that of the mode 2 of shape oscillations. These oscillations yield local changes in the curvature of the bubble surface, which results in modulations of the surface vorticity, hence in those of the strength of the streamwise vorticity injected in the wake, provided the decay rate of the oscillations is weak enough, i.e., the oscillatory Reynolds number $\mathrm{Ga}\,\mathrm{Bo}^{-1/2}$ is large enough.

Finally, DNS revealed the existence of a low-amplitude chaotic regime specific to the low-Morton-number range. This regime, where the lateral displacements of the bubble do not exceed $0.1D$, precedes the transition to the planar zigzagging or flattened spiraling regime. Hence, in that case the first bifurcation of the system breaks all possible symmetries, some of which are recovered through the next bifurcation. From the stability viewpoint, the important characteristic of this regime is that it is observed in a region of the parameter space where no standing eddy exists at the back of the bubble. Hence this is a clear case in which path instability does not result from a wake instability but rather from an instability intrinsic to the coupled bubble-fluid system, as already found with freely moving disks in some flow regimes where the wake is stable [65].

The onset of the instability takes place after the bubble has reached a quasiterminal rise velocity. However, there is in general a significant time delay between the two, during which the rise velocity displays a plateau, the length of which is an increasing function of the Bond number. This is the time period required for the attached eddy to grow and reach its "adult" size, then allowing wake instability to set in. The only exception is of course the transition to the low-amplitude chaotic regime that starts right after the bubble has reached its terminal velocity since there is no standing eddy in that case. Once path instability occurs, the rise velocity experiences a sharp decrease that can be up to approximately 10% of its previous value. This decrease results from both the wake-induced drag and the nonzero inclination of the instantaneous bubble velocity with respect to the vertical. Then, except in the pure helical regime, the above two mechanisms yield periodic or almost periodic oscillations of the rise velocity with a frequency twice that of the zigzagging motion and an amplitude that may in certain cases be up to 10% of U_T.

The role of shape oscillations in the transition to path instability appears to be complex. Since the larger the Bond number, the larger the deformation for a given value of the Galilei number, one might have expected time-dependent deformations to lower the threshold primarily for large Bond numbers. The DNS results are at odds with this intuition. Compared with the approximate critical curve obtained under the frozen-shape assumption, the threshold seems to be lowered when the Bond number is low ($\mathrm{Bo} < 1$), somewhat increased in the intermediate range $1 \leqslant \mathrm{Bo} \leqslant 5$, and unchanged when the Bond number is large enough ($\mathrm{Bo} \geqslant 5$). This suggests that these deformations trigger the instability at low Bond number but make the system more stable in the intermediate range because they help the bubble damp flow disturbances.

The present DNS results also helped reveal some general trends of the nonvertical regimes. For instance, for a given Mo, i.e., a given set of fluid properties, we found that the frequency of the horizontal movements is an increasing function of the distance to the threshold, i.e., of the bubble diameter. Similarly, for a given style of path, i.e., approximately a given distance $\mathrm{Ga} - \mathrm{Ga}_c$ to the threshold, this frequency was observed to increase with Mo. These trends are in line with available experimental and LSA results. More fundamentally, they follow the scaling of the vorticity flux generated at the bubble surface, which is at the root of path instability as soon as the latter is driven by a wake instability. Regarding the instability threshold, although the step between successive values of the Bond and Galilei numbers has to be reduced to obtain an accurate critical curve, the agreement between experimental data corresponding to well-controlled conditions and present DNS

predictions is satisfactory for Bo > 1. At lower Bo, the quantitative comparison is unfortunately obscured by the discovery of the low-amplitude chaotic regime.

Future progress in the intimate understanding of the mechanisms governing path instability requires further developments and massive use of DNS and LSA approaches. Regarding DNS, available techniques may be considered mature to describe the evolution of rising bubbles with $O(10^2)$ Reynolds numbers. In contrast, it must be kept in mind that achieving a faithful and thorough capture of all phenomena involved at the bubble surface when the Reynolds number is of $O(10^3)$ as it is in pure water remains a real challenge, in terms of both discretization methods and computational resources. This is especially true with fixed-grid approaches such as that employed here: Combining an accurate evaluation of the capillary force and of the very thin boundary layers that surround the bubble surface with a proper treatment of the large density and viscosity jumps in the same region remains a "Grail" of modern computational fluid dynamics and some improvements are certainly still required to make sure that the corresponding results are fully method independent. Besides these developments, repeating present computations on larger grids is necessary to assess and probably improve the accuracy on the position of the threshold $\mathrm{Ga}_c(\mathrm{Bo})$ in the region Bo $\lesssim 1$. Similarly, assessing the possibility that the primary bifurcation be subcritical requires series of runs in which the flow parameters are varied little by little to track possible hysteresis phenomena and bistability ranges, as recently achieved with various axisymmetric rigid bodies [64,67,71]. In parallel, the development of LSA codes in which the bubble surface is allowed to deform is needed to understand the possible role of transient shape deformations, especially regarding the threshold $\mathrm{Ga}_c(\mathrm{Bo})$ and the nature and characteristics of the first linearly unstable modes, through their coupling with the surrounding flow and the translational and rotational movements of the bubble. Once such codes will be available, it will become possible to develop weakly nonlinear models in the spirit of that of [22] to determine which path geometry is actually selected by the system close to the threshold.

ACKNOWLEDGMENTS

A major part of this work was supported by the Spanish MINECO, Subdireción General de Gestión de Ayudas a la Investigación, Junta de Andalucía and European Funds under Projects No. DPI2014-59292-C3-3-P and No. P11-TEP7495. Financial support from the University of Jaén, Grant No. UJA2015/06/14, is also acknowledged. The authors thank the Centro de Servicios de Informática y Redes de Comunicaciones of the University of Granada for providing computational resources and Dr. Benjamin Lalanne for helpful discussions regarding the computation of shape oscillations.

---

[1] C. D. Ohl, A. Tijink, and A. Prosperetti, The added mass of an expanding bubble, J. Fluid Mech. **482**, 271 (2003).
[2] W. L. Haberman and R. K. Morton, David Taylor Model Basin Report No. 802, 1953 (unpublished).
[3] R. Clift, J. R. Grace, and M. E. Weber, *Bubbles, Drops and Particles* (Academic, New York, 1978).
[4] A. W. G. De Vries, Path and wake of a rising bubble, Ph.D. thesis, University of Twente, 2001.
[5] C. H. J. Veldhuis, Leonardo's paradox: Path and shape instabilities of particles and bubbles. Ph.D. thesis, University of Twente, 2007.
[6] P. Ern, F. Risso, D. Fabre, and J. Magnaudet, Wake-induced oscillatory paths of bodies freely rising or falling in fluids, Annu. Rev. Fluid Mech. **44**, 97 (2012).
[7] P. G. Saffman, On the rise of small air bubbles in water, J. Fluid Mech. **1**, 249 (1956).
[8] T. Maxworthy, C. Gnann, M. Kürten, and F. Durst, Experiments on the rise of air bubbles in clean viscous liquids, J. Fluid Mech. **321**, 421 (1996).
[9] R. Zenit and J. Magnaudet, Path instability of rising spheroidal air bubbles: A shape-controlled process, Phys. Fluids **20**, 061702 (2008).

[10] R. Zenit and J. Magnaudet, Measurements of the streamwise vorticity in the wake of an oscillating bubble, Int. J. Multiphase Flow **35**, 195 (2009).
[11] A. Sato, Deformation, wake and collision of rising bubbles, Ph.D. thesis, Kyushu University, 2009.
[12] R. A. Hartunian and W. R. Sears, On the instability of small gas bubbles moving uniformly in various liquids, J. Fluid Mech. **3**, 27 (1957).
[13] H. Tsuge and S. I. Hibino, The onset conditions of oscillatory motion of single gas bubbles rising in various liquids, J. Chem. Eng. Jpn. **10**, 66 (1977).
[14] P. C. Duineveld, Rise velocity and shape of bubbles in pure water at high Reynolds number, J. Fluid Mech. **292**, 325 (1995).
[15] T. Sanada, K. Sugiara, M. Shirota, and M. Watanabe, Motion and drag of a single bubble in super-purified water, Fluid Dyn. Res. **40**, 534 (2008).
[16] J. Magnaudet and I. Eames, The motion of high-Reynolds number bubbles in inhomogeneous flows, Annu. Rev. Fluid Mech. **32**, 659 (2000).
[17] Y. Tagawa, S. Takagi, and Y. Matsumoto, Surfactant effect on path instability of a rising bubble, J. Fluid Mech. **738**, 124 (2014).
[18] J. Magnaudet and G. Mougin, Wake instability of a fixed spheroidal bubble, J. Fluid Mech. **572**, 311 (2007).
[19] B. Yang and A. Prosperetti, Linear stability of the flow past a spheroidal bubble, J. Fluid Mech. **582**, 53 (2007).
[20] J. Tchoufag, J. Magnaudet, and D. Fabre, Linear stability and sensitivity of the flow past a fixed oblate spheroidal bubble, Phys. Fluids **25**, 054108 (2013).
[21] G. Mougin and J. Magnaudet, Path Instability of a Rising Bubble, Phys. Rev. Lett. **88**, 014502 (2001).
[22] J. Tchoufag, D. Fabre, and J. Magnaudet, Weakly Nonlinear Model with Exact Coefficients for the Fluttering and Spiraling Motion of Buoyancy-Driven Bodies, Phys. Rev. Lett. **115**, 114501 (2015).
[23] J. C. Cano-Lozano, P. Bohorquez, and C. Martínez-Bazán, Wake instability of a fixed axisymmetric bubble of realistic shape, Int. J. Multiphase Flow **51**, 11 (2013).
[24] J. C. Cano-Lozano, J. Tchoufag, J. Magnaudet, and C. Martínez-Bazán, A global stability approach to wake and path instabilities of nearly oblate spheroidal rising bubbles, Phys. Fluids **28**, 014102 (2016).
[25] G. Mougin and J. Magnaudet, Wake-induced forces and torques on a zigzagging/spiralling bubble, J. Fluid Mech. **567**, 185 (2006).
[26] A. W. G. De Vries, A. Biesheuvel, and L. Van Wijngaarden, Notes on the path and wake of a gas bubble rising in pure water, Int. J. Multiphase Flow **28**, 1823 (2002).
[27] D. Gaudlitz and N. A. Adams, Numerical investigation of rising bubble wake and shape variations, Phys. Fluids **21**, 122102 (2009).
[28] J. Zhang and M.-J. Ni, Direct simulation of single bubble motion under vertical magnetic field: Paths and wakes, Phys. Fluids **26**, 102102 (2014).
[29] M. K. Tripathi, K. C. Sahu, and R. Govindarajan, Dynamics of an initially spherical bubble rising in quiescent liquid, Nat. Commun. **6**, 6268 (2015).
[30] S. Popinet, Gerris: A tree-based adaptive solver for the incompressible Euler equations in complex geometries, J. Comput. Phys. **190**, 572 (2003).
[31] J. C. Cano-Lozano, R. Bolaños-Jiménez, C. Gutiérrez-Montes, and C. Martínez-Bazán, The use of volume of fluid technique to analyze multiphase flows: Specific case of bubble rising in still liquids, Appl. Math. Model. **39**, 3290 (2015).
[32] S. Popinet, An accurate adaptive solver for surface-tension-driven interfacial flows, J. Comput. Phys. **228**, 5838 (2009).
[33] Sir H. Lamb, *Hydrodynamics*, 6th ed. (Cambridge University Press, Cambridge, 1932).
[34] A. Prosperetti, Normal mode analysis for the oscillations of a viscous liquid drop in an immiscible liquid, J. Méc. **19**, 149 (1980).
[35] D. I. Meiron, On the stability of gas bubbles rising in an inviscid fluid, J. Fluid Mech. **198**, 101 (1989).
[36] B. Lalanne, Simulation numérique directe de la déformation, des oscillations et de la rupture d'une bulle en ascension dans un écoulement instationnaire, Ph.D. thesis, Institut National Polytechnique de Toulouse, 2012.

[37] B. Lalanne, S. Tanguy, and F. Risso, Effect of rising motion on the damped shape oscillations of drops and bubbles, Phys. Fluids **25**, 112107 (2013).
[38] M. Horowitz and C. H. K. Williamson, The effect of Reynolds number on the dynamics and wakes of freely rising and falling spheres, J. Fluid Mech. **651**, 251 (2010).
[39] L. G. Leal, Vorticity transport and wake structure for bluff-bodies at finite Reynolds number, Phys. Fluids A **1**, 124 (1989).
[40] G. K. Batchelor, *An Introduction to Fluid Dynamics* (Cambridge University Press, Cambridge, 1967).
[41] A. Blanco and J. Magnaudet, The structure of the axisymmetric high-Reynolds number flow around an ellipsoidal bubble of fixed shape, Phys. Fluids **7**, 1265 (1995).
[42] P. C. Fernandes, P. Ern, F. Risso, and J. Magnaudet, On the zigzag dynamics of freely moving axisymmetric bodies, Phys. Fluids **17**, 098107 (2005).
[43] C. Brücker, Structure and dynamics of the wake of bubbles and its relevance for bubble interaction, Phys. Fluids **11**, 1781 (1999).
[44] J. Jeong and F. Hussain, On the identification of a vortex, J. Fluid Mech. **285**, 69 (1995).
[45] T. A. Johnson and V. C. Patel, Flow past a sphere up to a Reynolds number of 300, J. Fluid Mech. **378**, 19 (1999).
[46] P. Ploumhans, G. S. Winckelmans, J. K. Salmon, A. Leonard, and M. S. Warren. Vortex methods for direct numerical simulation of three-dimensional bluff body flows: application to the sphere at Re = 300, 500, and 1000, J. Comput. Phys. **178**, 427 (2002).
[47] J. Yang, G. Wu, W. Zhong, and M. Liu, Numerical study on bifurcations in the wake of a circular disk, Int. J. Comput. Fluid Dyn. **28**, 187 (2014).
[48] A. R. Shenoy and C. Kleinstreuer, Flow over a thin circular disk at low to moderate Reynolds numbers, J. Fluid Mech. **605**, 253 (2008).
[49] J. I. Jiménez-González, E. Sanmiguel-Rojas, and C. Martínez-Bazán, Laminar flow past a spinning bullet-shaped body at moderate angular velocities, J. Fluids Struct. **43**, 200 (2013).
[50] J. I. Jiménez-González, A. Sevilla, E. Sanmiguel-Rojas, and C. Martínez-Bazán, Global stability analysis of the axisymmetric wake past a spinning bullet-shaped body, J. Fluid Mech. **748**, 302 (2014).
[51] C. Veldhuis, A. Biesheuvel, and L. Van Wijngaarden, Shape oscillations on bubbles rising in clean and in tap water, Phys. Fluids **20**, 040705 (2008).
[52] T. Sanada, M. Shirota, and M. Watanabe, Bubble wake visualization by using photochromic dye, Chem. Eng. Sci. **62**, 7264 (2007).
[53] T. Saito and M. Toriu, Effects of a bubble and the surrounding liquid motions on the instantaneous mass transfer across the gas-liquid interface, Chem. Eng. J. **265**, 164 (2015).
[54] S. C. Crow, Stability theory for a pair of trailing vortices, AIAA J. **8**, 2172 (1970).
[55] J. T. Lindt, On the periodic nature of the drag of a rising bubble, Chem. Eng. Sci. **27**, 1775 (1972).
[56] K. Lunde and R. J. Perkins, Shape oscillations of rising bubbles, Appl. Sci. Res. **58**, 387 (1998).
[57] D. Fabre, F. Auguste, and J. Magnaudet, Bifurcations and symmetry breaking in the wake of axisymmetric bodies, Phys. Fluids **20**, 051702 (2008).
[58] F. Auguste, D. Fabre, and J. Magnaudet, Bifurcations in the wake of a thick circular disk, Theor. Comput. Fluid Dyn. **24**, 305 (2010).
[59] M. Jenny, J. Dusek, and G. Bouchet, Instabilities and transition of a sphere falling or ascending freely in a Newtonian fluid, J. Fluid Mech. **508**, 201 (2004).
[60] M. Chrust, G. Bouchet, and J. Dušek, Parametric study of the transition in the wake of oblate spheroids and flat cylinders, J. Fluid Mech. **665**, 199 (2010).
[61] W. Zhou and J. Dušek, Chaotic states and order in the chaos of the paths of freely falling and ascending spheres, Int. J. Multiphase Flow **75**, 205 (2015).
[62] K. Lunde and R. J. Perkins, *ASME Fluids Engineering Division Summer Meeting* (ASME, New York, 1997), paper FEDSM97-3530.
[63] F. Giannetti and P. Luchini, Structural sensitivity of the first instability of the cylinder wake, J. Fluid Mech. **581**, 167 (2007).
[64] F. Auguste, J. Magnaudet, and D. Fabre, Falling styles of disks, J. Fluid Mech. **719**, 388 (2013).

[65] J. Tchoufag, D. Fabre, and J. Magnaudet, Global linear stability analysis of the wake and path of buoyancy-driven disks and thin cylinders, J. Fluid Mech. **740**, 278 (2014).
[66] D. Fabre, P. Assemat, and J. Magnaudet, A quasi-static approach to the stability of the path of heavy bodies falling within a viscous fluid, J. Fluids Struct. **27**, 758 (2011).
[67] M. Chrust, G. Bouchet, and J. Dusek, Effect of solid body degrees of freedom on the path instabilities of freely falling or rising flat cylinders, J. Fluids Struct. **47**, 55 (2014).
[68] D. W. Moore, The velocity of rise of distorted gas bubbles in a liquid of small viscosity, J. Fluid Mech. **23**, 749 (1965).
[69] N. M. Aybers and A. Tapucu, The motion of gas bubbles rising through stagnant liquid, Wärme-Stoffübertragung **2**, 118 (1969).
[70] W. L. Shew, S. Poncet, and J.-F. Pinton, Force measurements on rising bubbles, J. Fluid Mech. **569**, 51 (2006).
[71] M. Chrust, G. Bouchet, and J. Dusek, Numerical simulation of the dynamics of freely falling discs, Phys. Fluids **25**, 044102 (2013).
[72] D. Fabre, J. Tchoufag, and J. Magnaudet, The steady oblique path of buoyancy-driven disks and spheres, J. Fluid Mech. **707**, 24 (2012).
[73] P. C. Fernandes, F. Risso, P. Ern, and J. Magnaudet, Oscillatory motion and wake instability of freely rising axisymmetric bodies, J. Fluid Mech. **573**, 479 (2007).